111-74

174956
p.48

NASA
Technical
Memorandum

NASA TM - 108410

DEVELOPMENT OF A LARGE FIELD-OF-VIEW KD*P MODULATOR--CENTER DIRECTOR'S DISCRETIONARY FUND FINAL REPORT (PROJECT NO. 91-23)

By E. A. West

Space Science Laboratory
Science and Engineering Directorate

June 1993

National Aeronautics and
Space Administration

George C. Marshall Space Flight Center

REPORT DOCUMENTATION PAGE

Form Approved
OMB No. 0704-0188

1. AGENCY USE ONLY (Leave blank)	2. REPORT DATE	3. REPORT TYPE AND DATES COVERED
	June 1993	Technical Memorandum

4. TITLE AND SUBTITLE
Development of a Large Field-of-View KD*P Modulator -- MSFC Center Director's Discretionary Fund Final Report (Project No. 91-23)

5. FUNDING NUMBERS

6. AUTHOR(S)
E. A. West

7. PERFORMING ORGANIZATION NAME(S) AND ADDRESS(ES)
George C. Marshall Space Flight Center
Marshall Space Flight Center, AL 35812

8. PERFORMING ORGANIZATION REPORT NUMBER

9. SPONSORING / MONITORING AGENCY NAME(S) AND ADDRESS(ES)
National Aeronautics and Space Administration
Washington, D.C. 20546

10. SPONSORING / MONITORING AGENCY REPORT NUMBER
NASA TM-108410

11. SUPPLEMENTARY NOTES
Prepared by Space Science Laboratory, Science & Engineering Directorate.

12a. DISTRIBUTION / AVAILABILITY STATEMENT
Unclassified--Unlimited

12b. DISTRIBUTION CODE

13. ABSTRACT (Maximum 200 words)

Magnetographs, which measure polarized light, allow solar astronomers to infer the magnetic field intensity on the Sun. The Marshall Space Flight Center (MSFC) Vector Magnetograph is such an imaging instrument. The instrument requires rapid modulation between polarization states to minimize seeing effects. The accuracy of those polarization measurements is dependent on stable modulators with small field-of-view errors. Although these devices are very important in ground-based telescopes, extending the field of view of electro-optical crystals such as KD*Ps (potassium di-deuterium phosphate) could encourage the development of these devices for other imaging applications. This report describes the work that was done at MSFC as part of the Center Director's Discretionary Fund (CDDF) to reduce the field-of-view errors of instruments that use KD*P modulators in their polarimeters.

14. SUBJECT TERMS	15. NUMBER OF PAGES
Polarization, Polarization Modulators, Electro-Optics, Polarized Light	48
	16. PRICE CODE: NTIS

17. SECURITY CLASSIFICATION OF REPORT	18. SECURITY CLASSIFICATION OF THIS PAGE	19. SECURITY CLASSIFICATION OF ABSTRACT	20. LIMITATION OF ABSTRACT
Unclassified	Unclassified	Unclassified	Unlimited

TABLE OF CONTENTS

LIST OF ILLUSTRATIONS

LIST OF TABLES

DEFINITION OF SYMBOLS

δ	the desired modulator retardance
δ_e	the error in the retardance
λ	wavelength of light
n_e	extraordinary index of refraction
n_o	ordinary index of refraction
n_x ($n_{x'}$)	index of refraction along the x (x') axis
n_y ($n_{y'}$)	index of refraction along the y (y') axis
n_z ($n_{z'}$)	index of refraction along the z (z') axis
Δ_x	the difference in the index of refraction (x axis) for light traveling in the z direction and z' direction
Δ_y	the difference in the index of refraction (y axis) for light traveling in the z direction and z' direction
z	this direction is the optic axis for the KD*P with no applied field
z'	this is the propagation direction for light traveling through the modulator
E_x ($E_{x'}$)	x (x') axis electric vector for light traveling in the z (z') direction
E_y ($E_{y'}$)	y (y') axis electric vector for light traveling in the z (z') direction
d_z ($d_{z'}$)	thickness of the crystal in the z (z') direction
$[I, Q, U, V]$	Stokes vector describing polarized light
I	intensity
Q	linear polarization intensity parallel to the analyzer
U	linear polarization intensity at 45° to the analyzer
V	circular polarization
$[\hat{q}, \hat{u}, \hat{v}]$	unit vectors on the Q, U and V axes of Poincaré sphere
P_Q	percentage of $+Q$ polarization from source
P_U	percentage of $+U$ polarization from source
P_V	percentage of $+V$ polarization from source
D_Q	difference array when the B image is subtracted from an A and 100% $+Q$ polarization is incident on the modulator
D_U	difference array when the B image is subtracted from an A and 100% $+U$ polarization is incident on the modulator
D_V	difference array when the B image is subtracted from an A and 100% $+V$ polarization is incident on the modulator
A	image created by the initial modulator voltage
B	image created by the second modulator voltage

STANDARD ABBREVIATIONS

MgF_2	magnesium fluoride
KD*P	potassium dideuterium phosphate

NONSTANDARD ABBREVIATIONS

LFOV	Large Field-of-View

UNUSUAL TERMS

The following names were given to the modulator designs used in this study. In the simple modulator designs, the modulator names are not abbreviated but are listed here for completeness.

Modulator name	Description
single KD*P	a single KD*P crystal which is used as the reference modulator.
single MgF_2	a single MgF_2 crystal whose optic axis is aligned parallel to a single KD*P crystal.
split MgF_2	two MgF_2 crystals are placed on each side of a single KD*P crystal.
crossed KD*P	two KD*P crystals with their fast axes crossed. Two halfwave plates with their fast axes at 22.5° and 67.5°
crossed MgF_2	the same components as the *crossed* KD*P modulator except that MgF_2 plates are placed on each side of the two KD*Ps.

TECHNICAL MEMORANDUM

DEVELOPMENT OF A LARGE FIELD-OF-VIEW KD*P MODULATOR (CENTER DIRECTOR'S DISCRETIONARY FUND FINAL REPORT) (PROJECT NUMBER 91-23)

I. INTRODUCTION

Polarized light allows researchers to remotely study the nature of the physical medium emitting or absorbing that light. In solar astronomy the scientist cannot measure the Sun's magnetic field in situ, but by using the Zeeman effect, the polarized light measured by a ground-based telescope can be related to the magnetic field strength and direction on the Sun. Since solar activity is related to the vector magnetic field on the Sun, the measurement of polarized light is an important tool in solar research. Therefore, the development of stable polarization modulators that have long lifetimes and a "large" field-of-view (LFOV) is important in ground-based observations of solar magnetic fields.

This report will discuss work that is being performed at the Marshall Space Flight Center to increase the field-of-view of KD*P modulators. The second section will describe the field-of-view limitations of electro-optical crystals and the two techniques that can be used to increase their field-of-view. These techniques work well when zero voltage is applied to longitudinal KD*Ps but cannot eliminate the field-of-view errors when voltage is applied to them. The third section will discuss the computer simulations for five different KD*P modulator designs, four of which have extended field-of-view properties. Based on the computer simulations, a modulator design will be selected and tested in the last section to confirm the results of the computer modeling.

II. DISCUSSION

In order to understand the field-of-view errors in birefringent crystals one must understand how the index of refraction varies in the crystal, how the optical engineer uses that property to study polarized light, and how that same property restricts the field-of-view of the instrument. In order to visualize these errors the index ellipsoid (Klein, 1970) is used to show how the index of refraction varies with direction. The difference in the major and minor axes of the ellipse describing the refractive indices creates a phase shift (retardation) in the electric vector components that describes the incident polarization. The Poincaré sphere (Shurcliff, 1966) then shows how that incident polarization and the retardation of the birefringent crystal interact with an analyzer.

In reality field-of-view "errors" are related to the natural properties of birefringent crystals and are not errors at all. When the instrumentalist uses this birefringent property in a collimated beam to create phase shifts in the incident polarized light there are no errors. In imaging systems, the "error" occurs when the

retardation is assumed to be constant although the angle of incident of the polarized light on the birefringent crystal varies. This error is systematic and, in some applications, can be corrected in the data analysis. Normally the optical engineer tries to minimize this systematic error by limiting the angle of incidence of the light on the crystal. When this approach cannot minimize the field-of-view error to an acceptable level, other crystals can be added to the optical system at special orientations or with opposite birefringence properties to cancel the "off-axis" phase shift error.

In order to visualize how this systematic error varies with the angle of incident, an ellipsoid can be used to describe how the index of refraction varies with direction. Figure 1 shows an ellipsoid where the principal axes are given by n_x, n_y, and n_z. Let E_x and E_y represent the electric vector components for polarized light traveling in the z direction. Then the phase shift in the electric vectors (E_x, E_y), is related to the difference in the indices of refraction $(n_x - n_y)$ by the following equation:

$$\delta = \frac{2\pi d_z (n_x - n_y)}{\lambda}$$

where d_z is the thickness of the crystal in the z direction. In Figure 1 the intersection of a plane perpendicular to the z axis and the index ellipsoid form an ellipse whose major and minor axes are n_x and n_y. The major and minor axes are also referred to as the slow and fast axes.[1]. In general, light propagating in any direction (z') in a birefringent crystal will also form an ellipse $(n_{x'}, n_{y'})$ which will determine how a given polarization will interact with that crystal.

Biaxial crystals represent the general case described above where the principal axes of the index ellipsoid are not equal $(n_x \neq n_y \neq n_z)$. Carefully studying the ellipsoid, an observer will find that there are two directions in which the intersection of a plane with the ellipsoid will form a circle $(n_{x'} = n_{y'})$. Since the optic axis of a crystal is defined as the direction in which the indices of refraction are equal, biaxial crystals have two optic axes. In their natural states both KD*P and MgF_2 crystals are uniaxial crystals where $n_x = n_y$. When a KD*P crystal is exposed to a strong electric field, the crystal becomes biaxial. Figure 2 shows the polarization patterns that will be seen when observing a KD*P between crossed polarizers. The images in Figures 2a and 2b represent polarization patterns that will be seen when a zero voltage is applied to the crystal and when the optic axis is parallel to the incident light. Figure 2a shows the KD*P crystal between crossed circular polarizers; Figure 2b crossed linear polarizers. Circular polarization allows the observer to readily identify the optic axis for uniaxial (and biaxial) crystals. When there is zero voltage on the KD*P, the indices n_x and n_y are equal to the "ordinary" index of refraction (n_o) for KD*P while the n_z index is equal to the extraordinary index (n_e). The nominal values for the ordinary and extraordinary indices of refraction for KD*P and MgF_2 crystals are given in Table 1. The electro-optic coefficient, which relates

[1] The larger the value of the index of refraction the slower the light travels through the crystal.

the change in the ordinary "indices" of refraction (n_x, n_y) with the applied voltage, has been described in greater detail elsewhere (West, 1978) and will not be discussed here. The main points to remember are: (1) that a zero applied voltage ($V = 0$) produces primary "indices" that are equal ($n_x = n_o = n_y$), (2) that the electro-optic coefficient allows a "positive" voltage ($+V$) to transform a KD*P into a biaxial crystal ($n_x < n_o < n_y$; Figure 2c), and (3) that changing the sign of the applied voltage ($-V$) reverses the inequality ($n_x > n_o > n_y$; Figure 2d).

Given that the indices of refraction change with the incident angle (and applied voltage), the Poincaré sphere is a useful tool to visualize how these retardation errors affect polarized light. Therefore, a short description of the Poincaré sphere (Shurcliff, 1966) and the Stokes vector is given.

The Stokes vector $[I, Q, U, V]$ provides a complete description for light entering or exiting an optical system: I represents the intensity of the light, $+Q$ is the linear polarization oriented at 0° to a defined direction, $+U$ is the linear polarization at 45° to that direction, and $+V$ represents left circular polarization.

The Poincaré sphere (Figure 3) provides a visual representation for the components of the Stokes vector. Linear polarizations are mapped along the equator of the Poincaré sphere, and the equatorial positions of $[Q, U]$ have the following definitions: $0°(+Q)$, $90°(+U)$, $180°(-Q)$, and $-90°(-U)$. Thus, the angular positions on the equator are equal to twice the angular orientations of the linear polarizations (e.g., $+U$ is at the equatorial position of +90° and represents linear polarization at 45°). Left and right circular polarizations (+ and $-V$) are located at the upper and lower poles of the sphere, respectively. Elliptical polarizations are mapped at all other points on the sphere according to the degree of ellipticity and the orientation of the major axis of the ellipse.

The Poincaré sphere also provides a visual technique to describe the action of a retarder. If the fast axis of a linear retarder is oriented at an angle θ with respect to the $+Q$ orientation, then its effect on any state of polarized light is determined by rotating the Poincaré sphere clockwise about the $+Q$, $-Q$ axis, where the rotation is through an angle given by the retardance (δ) of the waveplate. This rotation moves each point on the sphere to a new location which describes its new state of polarization. Thus, transforming left circularly polarized light ($+V$) to linearly polarized light at $0°(+Q)$ requires a clockwise rotation of the sphere through an angle of 90° about a diameter intersecting the point $-U$. In Figure 3 the fast axis for a quarterwave retarder is labeled **R** and the retardance $\delta_{\mathbf{R}}$. Since the Poincaré sphere is a three-dimensional object which is difficult to visualize on the printed page, snapshots from a particular direction will usually be added to help see the back or side views of the Poincaré sphere. The fast axis of the optical components will be labeled on the Poincaré sphere while the retardances will be labeled on the two-dimensional snapshots of the sphere.

A. Correcting the Natural Birefringence Field-of-View Errors

The index ellipsoid describes how the indices of refraction vary with the angle of incidence in birefringent crystals. This variation of the index of refraction with the incident angle explains why the field-of-view of electro-optic crystals must be limited or errors will occur. The field-of-view errors for a longitudinal KD*P modulator with zero applied voltage are created by the extraordinary (n_e, n_z) index of refraction. Two techniques have been discussed that minimize the field-of-view errors in KD*P modulators (West, 1978; Guo-Xaing and Yue-Feng, 1981). In the first technique two KD*Ps have their voltage induced fast axes crossed like "zero" order[2] waveplates. In the second technique, a positive uniaxial crystal, magnesium fluoride (MgF_2), has its optic axis aligned parallel to the optic axis of the longitudinal KD*P modulator (a negative uniaxial crystal).

The Poincaré sphere will now be used to show how two KD*Ps can be optically aligned to eliminate their field-of-view errors created by their natural birefringence. Since the optic axis of the KD*Ps is parallel to the "incident" light, the indices of refraction are the same for both KD*Ps ($n_x = n_y$) and there is no change in the incident polarization. As described earlier the retardance for light traveling in the z' direction is related to the difference in the indices of refraction $(n_{x'} - n_{y'})$ and the distance traveled $(d_{z'})$. The fast axis can be either $n_{x'}$ or $n_{y'}$. If light traveling in the z' direction is linear polarized with its electric vector vibrating in either the $n_{x'}, n_{z'}$ plane or the $n_{y'}, n_{z'}$ plane, there will be no change in the polarization of the light. Since there is no change in the incident polarization the observer might conclude that there is no field-of-view errors in that direction. This conclusion is wrong. Some linear polarizations may align with the *local*[3] fast or slow axis and the retardation errors will not change that polarization. Therefore, crossed circular polarizers are used in the Poincaré simulations.

Figure 4 shows how circularly polarized light traveling in the z' direction will undergo a small phase shift $(\delta_{\mathbf{K_1}})$ from a single KD*P whose optic axis is in the z direction and whose *local* fast axis $(\mathbf{K_1})$ is at $+Q$. If a second KD*P is added with the same optical alignment and thickness, its fast axis $(\mathbf{K_2})$ and phase shift $(\delta_{\mathbf{K_2}})$ will be the same as that of the first KD*P. Therefore, the field-of-view errors for two KD*Ps are twice as large as that of a single KD*P.

In Figure 5 two halfwave plates $(\delta_{\mathbf{H_1}} = \delta_{\mathbf{H_2}} = 180°)$ are placed between the two KD*Ps with their fast axes at $[+U + 22\frac{1}{2}°]$ $(\mathbf{H_1})$ and at $[+U - 22\frac{1}{2}°]$ $(\mathbf{H_2})$. These waveplates rotate the elliptical polarization created by the field-of-view errors of the

---

[2] Zero order is the term used in most sales catalogs for high quality waveplates that have a minimum sensitivity to temperature, wavelength, and angle of incidence. Depending on ones approach, the terms "first" order and "zero" order can represent the same waveplate. In this report the order (m) of a waveplate with a given retardance (δ) is related to the difference in the retardance of the two plates $(m + \delta = \delta_1 - \delta_2, m = 0, 1, 2...)$.

[3] In order to minimize the confusion in describing *off-axis* fast/slow axis or *off-axis* optic axis, the term *local* is used in place of *off-axis*.

first KD*P to an elliptical polarization which when incident on the second KD*P is transformed back to circular polarization ($+V$). Therefore, when looking at this modulator between crossed circular (or linear) polarizers, the halfwave plates have eliminated the KD*P field-of-view errors. This will be demonstrated in section III in the *crossed* KD*P modulator simulations. The next section will describe how this technique is affected when a voltage is applied to the KD*Ps.

The second technique that is used to minimize the field-of-view errors of KD*Ps is to co-align the optic axes of a KD*P and a MgF_2 crystal. Figure 6 shows the Poincaré sphere for this situation. KD*P crystals are negative "uniaxial" crystals ($n_e - n_o < 0$) while MgF_2 crystals are positive. For positive uniaxial crystals the off-axis indices of refraction are related to the original indices in the following way: $n_{x'} = n_o + \Delta_x(z')$ and $n_{y'} = n_o + \Delta_y(z')$. For negative uniaxial crystals the indices of refraction are: $n_{x'} = n_o - \Delta_x(z')$ and $n_{y'} = n_o - \Delta_y(z')$. Therefore, for light at a given direction z', the field-of-view errors have opposite signs in the two crystals. The main problem in this technique is in matching the thickness of the MgF_2 crystal such that its off-axis errors (δ_M) are equal to the off-axis errors of the KD*P crystal. In Figure 6 the off-axis error of the KD*P (δ_K) changes the incident circular polarization ($+V$) to an elliptical polarization. If the thickness of the MgF_2 plate is optically matched to the KD*P, the off-axis error of the MgF_2 (δ_M) should change the elliptical polarization created by the KD*P back to the incident circular polarization. In section III this modulator will be referred to as the *single* MgF_2 modulator.

B. Understanding the Applied Voltage field-of-view Errors

The techniques described in the last section work well when zero voltage is applied, but all applications using KD*Ps *modulators* required a minimum of two retardation states (i.e., $A = 0°$, $B = 90°$) This section will describe how applying an electric field in the z direction distorts the natural birefringence and reduces the field-of-view corrections for the techniques described in the previous section.

When a voltage is applied to a longitudinal (z direction) KD*P crystal, the indices of refraction for light traveling in that direction are $n_x = n_o + \epsilon_v$ and $n_y = n_o - \epsilon_v$, where ϵ_v represents the change in the ordinary index of refraction when a voltage v is applied. With the applied voltage the KD*P crystal becomes a biaxial crystal (Figures 2c and 2d). Unfortunately, MgF_2 crystals are not sensitive to voltage and, at this time, there are no known positive uniaxial crystals with large electro-optic coefficients that could be used to minimize the applied voltage, field-of-view errors in KD*Ps. For **small** off-axis angles, the voltage induced change in the indices of refraction (ϵ_v) is assumed to be larger than the natural birefringence error. Therefore, in Figure 7 the voltage induced retardance of the KD*P rotates the $+V$ circular polarization to the $-V$ polarization on the Poincaré sphere. Now the MgF_2 plate, which corrects the zero voltage KD*P errors, limits the field-of-view by changing the $-V$ polarization to elliptical polarization.

The Poincaré sphere in Figure 8 shows the on-axis response of a *crossed* KD*P modulator with a quarterwave retardance between crossed circular polarizers. For

small incident angles where the change in the indices of refraction from the applied electric field is larger than the off-axis errors, the halfwave plates will continue to correct the retardation errors in the KD*Ps. At larger angles the error in the indices (Δ_x, Δ_y) will have the same sign for both KD*Ps which will create a retardance error ($\delta_e(z')$) with same sign, **but** the magnitude of the retardance error will be different. Since the retardance error is different, the *crossed* KD*P modulator has a limited field-of-view, but this design appears to represent the best approach for correcting the field-of-view errors when voltage is applied.

Although the index ellipsoid and the Poincaré sphere is used to study selected directions, trying to map a large area is difficult and time consuming. In order to study the optical properties of the different modulators considered in this report, computer simulations were developed to calculate the field-of-view characteristics for the different optical elements as a function of temperature, wavelength, optic axis orientation, fast axis alignment, crystal thickness, and applied voltage. These simulations will be described in the next section.

III. COMPUTER SIMULATIONS

The equations that were used in the computer simulations are developed in Appendix A. This section will be limited to describing the results of the computer simulations on five different KD*P modulators.

These simulations are based on the MSFC vector magnetograph requirements (Hagyard, et al., 1984; West, 1985) where an unknown polarization must be quickly modulated between two polarization states with a total phase shift between those states of 180°. This allows the modulator to have a zero to halfwave (0° to 180°) modulation scheme or a plus, minus quarterwave (−90° to +90°) modulation. Although some applications may require only a small change in the retardance, this requirement for a 180° phase shift represents the worst case for most "normal" longitudinal KD*P applications. The simulations assume that the modulators are in a collimated light source. For an imaging instrument this simply means that each point in the image has a collimated beam associated with it but that the incident angle of the collimated beam on the modulator will vary for each point in the image. Assuming perfect parallel plates and neglecting edge effects, the collimated beam requirement simplifies the ray tracing for the $E_{x'}$ and $E_{y'}$ components of the incident light.

Comparing polarization images from different modulators can be deceiving. An error may exist but the alignment of the polarization with the local "fast axis" may not create a phase shift and the error will go unnoticed.[4] Although crossed circular polarizers represent the best technique for displaying the retardation errors of simple modulators, two of the designs that will be considered use retarders between the KD*P modulators. This produces polarization images whose output

[4] The elliptical (circular) patterns in Figure 2 are related to the retardance variation while the straight lines (cross) are related to the alignment of the linear polarization to the "local" fast or slow axis.

intensity is dependent on the retardation and fast axis of the waveplates. Therefore, simply comparing the circular polarization maps of the retarder designs versus the no-retarder designs is difficult. The best method for comparing modulators is to study images created by polarizations "leaking" through the modulator due to the field-of-view errors. Therefore, polarization maps of $[I + Q]$, $[I + U]$, and $[I + V]$ for both modulator states were included in the simulations. Also a linear analyzer, which is the type used in the MSFC vector magnetographs, was used to generate these polarization images. One set of maps represents a "high/low" situation where one modulator voltage setting produces the maximum signal at the center of the field-of-view while the other voltage setting produces the minimum signal. The other polarization maps represent the "equal" signal situation where both modulator positions have a signal that is 50% of the maximum signal at the center of the field-of-view. The difference between the "equal" signal maps indicates the location and magnitude of the polarization crosstalk in the "high/low" polarization measurement.

A. Description of KD*P Modulators Used in Simulations

Figure 9 shows the optical components, the modulation scheme, and the measured polarization (assuming a linear analyzer at 0°) for the five modulators that were studied. The first two designs have been used in the existing MSFC vector magnetograph since 1983. The next three designs were included because of their possible application in the ground-based testing of EXperimental Vector Magnetograph (EXVM) that is being developed at Marshall. The assumed thickness of the KD*P crystals in all of the modulators is 3 mm.

The first modulator is a *single* KD*P which has no field-of-view correction and is used as the reference. Figure 10 shows the polarization images that will be seen through a linear analyzer if 100% linear (Q, U) or circular (V) polarization is incident on the crystal. The modulation scheme for this crystal is positive and negative quarterwave (± 1734 volts is equal to a ±90° retardance). Although a zero, halfwave modulation could have been selected for these simulations, large dc bias voltages on KD*Ps have been a problem in the past (West, 1989) and are not used in the Marshall magnetographs. The on-axis, maximum signal occurs when the incident polarization is $+V$ and a positive quarterwave retardance is applied to the crystal. Using this modulation scheme, the linear polarizations ($+Q$, $+U$) have the same *on-axis* signal (50% of the maximum). Subtracting the negative quarterwave image (B) from the positive quarterwave image (A) for the $+Q$ and $+U$ polarizations produces a zero signal at the center of the field-of-view. The difference between the A and B images indicate how much $+Q$ and $+U$ crosstalk can get into the $+V$ polarization measurement. For example, let the difference map for each polarization be defined as a two-dimensional array, $D_p(x, y)$, where $p = \{Q,\ U,$ or $V\}$. Let the polarization from the source be defined as $P_Q(x, y) = \frac{Q(x,y)}{I(x,y)}$, $P_U(x, y) = \frac{U(x,y)}{I(x,y)}$, and $P_V(x, y) = \frac{V(x,y)}{I(x,y)}$. Then the measured polarization, $P_m(x, y)$, from an unknown source would be related to the polarization source by the following equation:

$$P_m(x,y) = \frac{A-B}{A+B} = D_Q * P_Q\hat{q} + D_U * P_U\hat{u} + D_V * P_V\hat{v}$$

where $\hat{q}$, $\hat{u}$, and $\hat{v}$ are unit vectors along the Q, U, and V axes of the Poincaré sphere.[5] A is simply defined as the image created by the first retardation state for the KD*P modulator and B the second retardation state. In this example, the first polarization image is acquired when a positive quarterwave voltage is applied to the KD*P while the second image is a negative quarterwave voltage. In the vector magnetic field measurements at Marshall's Solar Observatory, the polarization images of the source are normally isolated in image (A/B) pairs so that only P_Q, P_U, or P_V are measured (West, 1985). With this modulator, the ***on-axis*** $(x = 0,\ y = 0)$ values of the difference arrays are: $D_Q(0,0) = 0$, $D_U(0,0) = 0$, and $D_V(0,0) = 1$. Therefore, the measured polarization (P_m) is equal to the circular polarization of the source (P_V). Since the field-of-view of the images in Figure 10 is $\pm 10°$, the D_Q and D_U maps imply that the field-of-view of a ***single*** KD*P should be less than $\pm 1°$ or significant crosstalk will exist in the polarization measurements.

In the original vector magnetograph, two KD*P crystals were used but the fast axes were separated by 45° so that the complete Stokes vector could be measured without any rotating components. A MgF_2 crystal was placed between the two KD*Ps to reduce the field-of-view errors (West, 1978). When the MSFC magnetograph was redesigned in 1983, a single KD*P with a matching MgF_2 plate was used in the new polarimeter. This modulator will be referred to as the ***single*** MgF_2 modulator. This device is still in use in the MSFC Vector Magnetograph. Figure 11 shows the polarization images and the difference arrays obtained by the modulation of the KD*P between positive and negative quarterwave voltages. When looking at the "big" picture, the images show a large improvement with almost the complete elimination of the circular ring structure. Although the D_Q image shows a significant improvement in the $+Q$ polarization crosstalk, the D_U image allows only a 40% increase in the field-of-view when compared to the ***single*** KD*P modulator.

The third modulator is a ***split*** MgF_2/KD*P design. Although neglected in the earlier work (West, 1978), this design was included because of its potential application in the new vector magnetograph (EXVM) that is being built at Marshall. The polarization images created by this modulator are shown in Figure 12. A significant improvement can be seen when comparing the D_Q and D_U polarization patterns of the ***split*** MgF_2 modulator to those of the ***single*** MgF_2 modulator (Figure 11). In Figure 7, the off-axis retardance for the KD*P is assumed to be small when compared to the voltage induced retardance. Therefore, the "main" off-axis error in Figure 7 is from the MgF_2 crystal (δ_M) (which corrects the zero voltage natural

[5] Although the "real" output from a detector is a scaler, the "vector" format is used to emphasize the crosstalk of two of the polarization sources into the desired polarization measurement. Although Mueller matrices are normally used to relate the measured polarization to the input polarization, the "vector" format seemed to be the best technique for describing the field-of-view errors (D_p) and their relationship to the input (P_p) and measured (P_m) polarization.

birefringence errors of the KD*P). By splitting the MgF_2 crystal (Figure 13), the polarization error created by the first MgF_2 (δ_{M_1}) is rotated to the opposite side of the Poincaré sphere by the KD*P (δ_K). The error from the second MgF_2 (δ_{M_2}) then rotates the polarization back to the desired position minimizing the field-of-view errors in this modulator.

The next KD*P modulator provided the initial stimulation for this new study into the field-of-view errors of KD*Ps. The concept that two KD*Ps (*crossed* KD*P modulator in Figure 9) could have a larger field-of-view than one KD*P did not, at first glance, appear logical. The Poincaré sphere in Figure 5 showed that this design did indeed create a modulator with no field-of-view errors when a zero voltage was applied. This is seen in the A images for the $+Q$, $+U$ and $+V$ polarization images in Figure 14. Because there are two KD*Ps, a zero to $\pm$ quarterwave modulation scheme will modulate the $+Q$ polarization signal between a minimum (A image) and maximum (B image) level. In this case the maximum signal occurs with a $+Q$ input polarization and a plus quarterwave on KD^*P_1 (negative quarterwave on KD^*P_2). [6] Since the A image is defined to be the zero applied voltage and the B image the quarterwave voltage, then the *on-axis* values for the difference images are $D_Q(0,0) = -1$, $D_U(0,0) = 0$, and $D_V(0,0) = 0$. Comparing the D_V and D_U images for this modulator with D_Q and D_U images for the single KD*P confirms the fact that the *crossed* KD*P modulator has a field-of-view that is at least two times larger than the *single* KD*P modulator. Comparing this design with the *single* MgF_2 modulator is a little more difficult. Looking only at the minimum/maximum signals ($+V$ polarization in Figure 11, $+Q$ polarization in Figure 14), the *single* MgF_2 modulator **might** appear to have a larger field-of-view than the *crossed* KD*P modulator. Unfortunately the large difference in the D_U image of the *single* MgF_2 modulator represents the true limit in its field-of-view. Therefore, the *crossed* KD*P design has the largest field-of-view. When the difference images of the *crossed* KD*P are compared with the *split* MgF_2 images (Figure 12), the *split* MgF_2 modulator appears to have best overall performance.

The last modulator combines the two techniques to see if any further improvement can be made. This modulator is referred to as the *crossed* MgF_2 design.[7] The polarization maps created by this design are shown in Figure 15. Although the MgF_2 crystals smooth out the outer fringes, the field-of-view does not appear to be any larger than the *crossed* KD*P modulator. The main reason for this is that the MgF_2 crystals and the halfwave plates have the same function, to eliminate the field-of-view errors when zero voltage is applied. Therefore, combining the techniques produces no improvement in the zero voltage condition, and, when a voltage is applied, the two techniques interact but little improvement is seen with this design. The next section will describe why this physical limit exists and why the *split* MgF_2 modulator was selected as the optimum modulator for use in the

[6] These voltages can be in the opposite order, negative on KD^*P_1, positive on KD^*P_2. This will create polarization images that will rotate 90° but this will have no effect on the overall field-of-view characteristics of the modulator.

[7] This is short for *crossed* KD*P modulator with MgF_2 crystals.

MSFC vector magnetographs.

B. Selection of a LFOV Modulator for Testing

Before describing the optical testing of the large field-of-view design that has been selected for use in the MSFC Vector Magnetograph, some comments should be made on the general characteristics of these LFOV designs. In every LFOV modulator, the field-of-view problems occur along the x and y axis but not along the diagonals ($x = y$ or $x = -y$). This is due to the fact that a **linear** analyzer at 0° was selected for these simulations. Rotating the analyzer will rotate the polarization images by the same amount. The second point that must be re-emphasized is that a linear analyzer may allow errors to go unobserved. The excellent D_Q/D_U difference images (Figure 12) for the *split* MgF_2 modulator does not mean that the field-of-view errors are gone, only that they are not detected with the linear analyzer. If the field-of-view errors did not exist, the difference map (D_V) for the *split* MgF_2 modulator would not vary over the image. This brings up an important point when comparing modulators. The square root of the sum of the squares of the difference images will not be equal to one over the full image ($[D_Q^2 + D_U^2 + D_V^2]^{\frac{1}{2}} \leq 1$). Figure 16 shows this characteristic for all of the modulators considered in this report. One interesting fact that this figure shows is that the *single* KD*P and the *crossed* KD*P modulators have the same total polarization maps (Figures 16a and 16d). This implies that the incident polarization signal can still be recovered using a *single* KD*P modulator if the field-of-view errors are known and corrected for in the data analysis. Another point that must be emphasized is that the minimums in these images map areas in which the incident polarization (P_Q, P_U, or P_V) signal will be lost and, in fact, the total polarization maps in Figure 16 represent the *true* field-of-view limitations for these modulators. Why is this polarization signal lost? What is happening at these minimum positions is that the fast or slow axis is parallel to the incident linear polarization. Therefore, there is no change in the input polarization. This can be verified by observing that minimums in Figure 16 are the transmission peaks in the $+Q$ polarization in Figures 11 and 12. Yet Figures 11 and 12 show very little signal in the D_Q maps. This means that, although the fast axis for the KD*P at the center of the field-of-view is at 45° to the analyzer, the fast (or slow) axis observed at these transmission peaks must be parallel to the electric vector of the $+Q$ polarization.

Sandwiching each KD*P with two MgF_2 plates allows us to change the *true* field-of-view limitations to those of the *split* and *crossed* MgF_2 designs (Figures 15c and 15e). This field-of-view improvement is $\approx \sqrt{2}$ over the *single* and *crossed* KD*P modulators.

At Marshall the approach has been to minimize the polarization crosstalk. The best way to compare modulators for crosstalk is to eliminate the high/low difference image from the square root of the sums calculation. For the *single* KD*P, *single* MgF_2, and *split* MgF_2 modulators $(D_Q^2 + D_U^2)^{\frac{1}{2}}$ is calculated; for the *crossed* KD*P and *crossed* MgF_2 modulators $(D_U^2 + D_V^2)^{\frac{1}{2}}$. These images are scaled linearly between 0 and 1 as shown in Figure 17. In order to see the polarization errors in the

split MgF_2 a roll over intensity scale has been used. Since the *split* MgF_2 modulator has the minimum total crosstalk, it has been selected as the optimum modulator for use in the MSFC vector magnetographs. The next section will discuss the optical testing of the this modulator.

IV. OPTICAL TESTING

The optical testing will be limited to the confirmation of the polarization images seen in Figure 12. A more detailed analysis will be given in a second paper.

A. Test Equipment

Figure 18 shows the optical equipment that was used in the testing of the *split* MgF_2 modulator. A multiline helium neon laser (Particle Measuring Systems, model LSTP-0010) was used as the source. Four wavelengths can be selected using this laser: 5430, 5941, 6119 and 6234 Å. The red wavelength, 6234 Å, has the highest output power and was used in most of the optical testing. A microscope lens with a pinhole was mounted in the front of the laser to create a diverging beam. A linear polarizer was then used to produce the input polarization for the KD*P modulators. Because of the limited space, sheet polaroids had to be used in the input polarizer and analyzer positions. Although some retardation errors will exist with these polarizers, these errors are small when compared to the field of view errors of the KD*P modulators. After the input polarizer, a second lens is used to focus the light onto the KD*P modulator. The lens has a focal length of 67 mm. Although faster lenses are possible, the placement of the modulator (or test samples) between the lens and the focal point simplifies the calibration for the thickness matching of the KD*P and MgF_2 crystals; unfortunately this limits the angular input to $\pm 8°$. The analyzer was then placed as close as possible to the KD*P modulator to be tested to minimize vignetting. Although film was used in some of the initial testing, the final testing was done using a standard RS170 video camera. A third lens was added to refocus the beam onto a Dage-MTI interline transfer CCD camera (model 72). Nuetral density and interference filters were then placed between the third lens and the CCD camera to optimize the video signal. This signal was then fed into a Sony video recorder (model VO 9600). After the modulator data was recorded, the video was fed into a video frame grabber which is part of the MSFC Vector Magnetograph facility. Selected frames were then digitized to document the performance of the KD*P modulators.

B. Polarization Measurements

The longitudinal KD*P modulators that were used in these tests were manufactured by Interactive Radiation, Inc. (INRAD) and had an aperture size of 30 mm. One of the main problems with building the *split* MgF_2 modulator is the thickness matching when zero voltage is applied. Since the KD*P crystal is between glass plates, measuring the thickness of the crystal must be done indirectly. This is done

by placing the KD*P sample into the optical setup shown in Figure 18, crossing the transmission axes of the two polarizers, and measuring the distance from the optic axis to the minimum polarization rings. The first ring represents a 180° retardance, second ring 360°, the third 540°, etc. Knowing this distance and the distance to the focal point gives you the exiting angle from the KD*P modulator. Assuming that the KD*P is the only source for this phase shift, the thickness of the KD*P can be estimated. The equations used to estimate the thickness of the KD*P crystal inside of the modulator are similar to those derived in Appendix A. In order to determine the accuracy of this technique, two KD*P crystals that were not mounted and whose thickness could be measured directly were also used in this test. As an additional confirmation of the thickness estimates, the measurements were made at the four HeNe wavelengths. The results from these tests are given in Table 2. For the test samples, 5-2 and 9-4, the difference in the 180° minimum and the 360° minimum thickness estimate is less than 0.1 mm. The measured thickness for these samples is 3.90 $\pm$0.05 mm for sample 5-2 and 2.95 $\pm$0.05mm for sample 9-4. Considering the limited number of samples and the error bars associated with this procedure, the agreement between the measured and the estimated thicknesses is quite good.

The main problem occurs when comparing the 180° and the 360° estimated thickness for the two modulators (12595-1, 12595-2). There appears to be a systematic difference of $\approx$ 0.07 mm. This systematic difference is *probably* due to the glass windows that are placed on each side of the KD*P crystal to protect it from humidity. Assuming that any systematic errors created by the glass windows would occur at the higher order minimums, the thicknesses of the MgF_2 crystals were selected to match the 180° minimums for the two modulators. Therefore, the thicknesses of the MgF_2 crystals to be used with KD*P's 12595-1 and 12595-2 were chosen to be 4.00 and 4.25 mm thick. Although the initial MgF_2 crystal had some stress birefringence and transmission loss, the polishing procedure was quickly determined and the samples that were obtained for this test program had very high contrast ratios.

C. Data Analysis

Most of the problems that were encountered in the KD*P testing were expected. The fringing produced by the neutral density filters, the lenses and the KD*P modulators created interference patterns that added to the polarization patterns produced by the field-of-view errors. Also the radial intensity dependency created by the diffraction of a point source (in the microscope lens) made comparisons between the calculated and acquired images difficult. These problems were expected and can be accounted for. On paper these problems can be corrected by removing the KD*P modulator to obtain a "photo-calibration." By removing the monochromatic fringing and diffraction patterns, the remaining errors should only be those associated with the natural birefringence of MgF_2 and KD*P crystals. Unfortunately the detector which was used was not linear and did not have adequate resolution over a large intensity range to see both the far field and small field errors. Also, normalizing the polarization patterns by intensity (i.e., $\frac{Q}{I}$ as in the computer

simulations) was not possible because of division by zero. Finally the computer simulations assumed perfect lenses, collimated light at various angles to the optic axis, and square pixels on the detector. All of these errors produced observed intensity patterns that were difficult to compare with the computer generated images shown in Figures 10 and 12. Therefore the computer simulations were recalculated to try to compensate for the detector distortion, linearity and saturation. Although these simulations are in better agreement, there are some differences between the calculated and observe polarization patterns that have not been resolved at this time. When the new EXVM detector system becomes operational, the polarization data will be reproduced so that the smaller errors that may exist in this data can be studied in detail. The EXVM camera system has a linear response to light, can be synchronized to the KD*P modulator, and has a larger dynamic range.

Figure 19 compares the field-of-view errors that were observed with the calculated polarization pattern when zero voltage is applied to the KD*P. The maximum field-of-view is approximately $\pm 8°$. The calculated image is the same as that shown in Figure 2b but with saturation occurring at 5% of the maximum intensity, the input polarization crossed to the analyzer, both linear polarizers rotated 23° and a 3 X 4 image distortion to match the video image. The point source illumination, the monochromatic fringing, and the exact plate scale of the detector have not been corrected for in the calculated images. The next two figures have exactly the same scale and format.

Figure 20 shows the polarization patterns that were observed for the *single* KD*P modulator and compares the observed difference image with the calculated difference. The difference images (Figures 20c and 20d) agree well near the optic axis but, as one goes to the outer edges of the field-of-view, the calculated image shows more structure than was observed. This is due to the use of a "point" source in the observed images, and the assumption in the calculated images that the ordinary and extraordinary rays recombine after exiting the modulator (implication is that the source is extended and collimated). Another problem that occurs in the observed polarization images is the saturation effects of the detector. A comparison of the difference pattern in Figure 20d with the $A - B$ image in the Q measurement in Figure 10 shows that large differences exist near the optic axis in Figure 10 but are zero in Figure 20d. This difference is related to the detector saturation. Therefore, saturation effects must be understood in order to correctly interpret the difference images shown in Figure 20.

Figure 21 shows the polarization patterns produced by the *split* MgF_2 modulator. Although the observed and calculated difference images (Figures 21c and 21d) show good agreement in the basic polarization image, there are more structures in the far field-of-view of the calculated image than in the observed images.

V. CONCLUSIONS

Although the acquired images and the computer simulations agree well when comparing the field-of-view errors in the different modulator designs, there are some improvements that can be done in the computer simulations to more accurately model the observed patterns. An optical ray trace of the lenses and neutral density filters would greatly aid in any comparison of the calculated and measured far field of view errors.

When the EXVM detector system becomes available, these measurements will be reproduced so that the effects of small polarization errors, such as stress birefringence (West and Bhatia, 1990), variation of the electric field over crystal (West and Wilkins, 1992), and retardation errors in the calibration optics, can be included in the LFOV modulator study.

The main conclusion from this study is that the split MgF_2 design provides the largest field-of-view with the minimum amount of polarization crosstalk. A simple comparison of the saturated border in the observed difference images of the *single* KD*P (Figure 20c) and the *split* MgF_2 (Figure 21c) modulators show that the field-of-view of the *split* MgF_2 design is four times larger than that of the single KD*P design. Therefore, this design will be used in the ground-based testing of the new vector magnetograph (EXVM) that is being developed at Marshall.

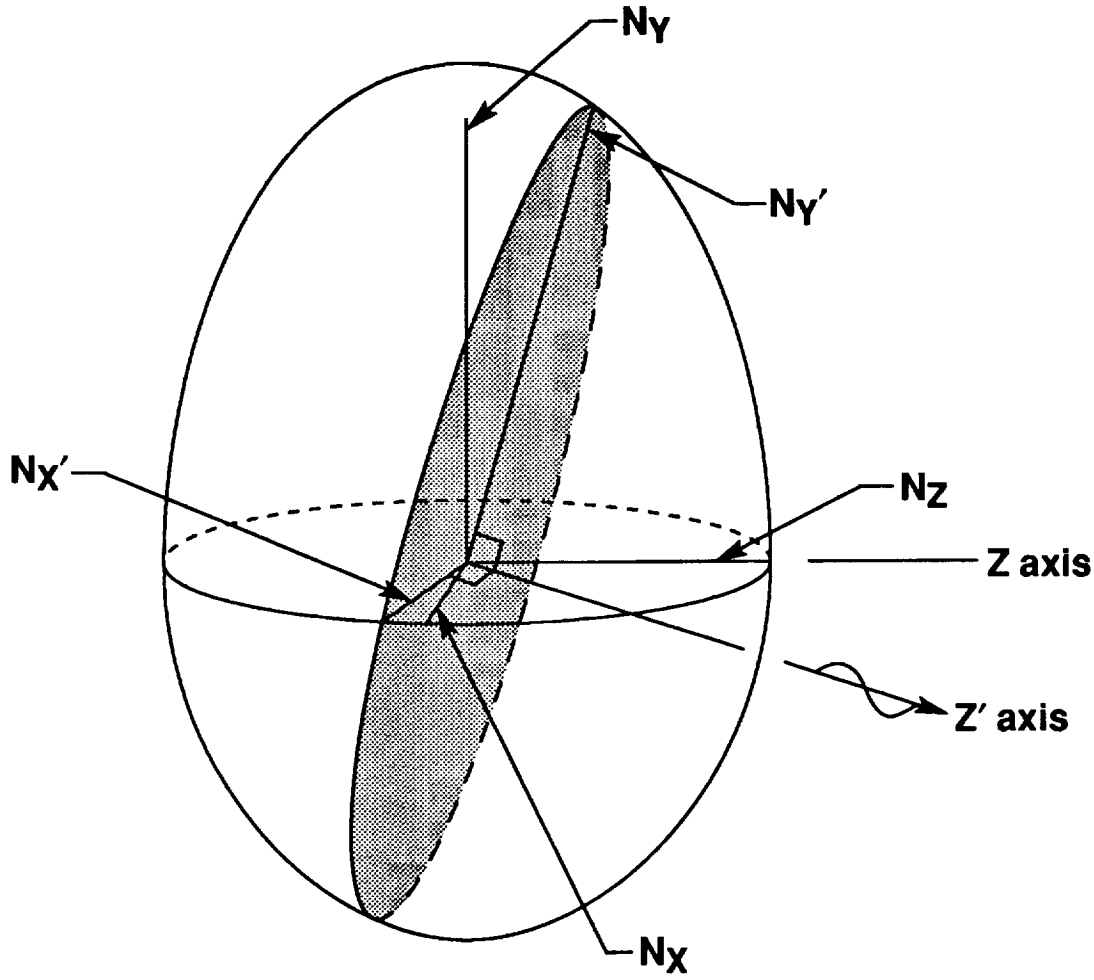

Figure 1. Index ellipsoid showing the principal indices of refraction, n_x, n_y and n_z. The indices of refraction for light traveling in the z' direction is determined by the intersection of a plane perpendicular to the propagation direction and the index ellipsoid. The intersection forms an ellipse whose minor (fast) and major (slow) axis are given by $n_{x'}$ and $n_{y'}$.

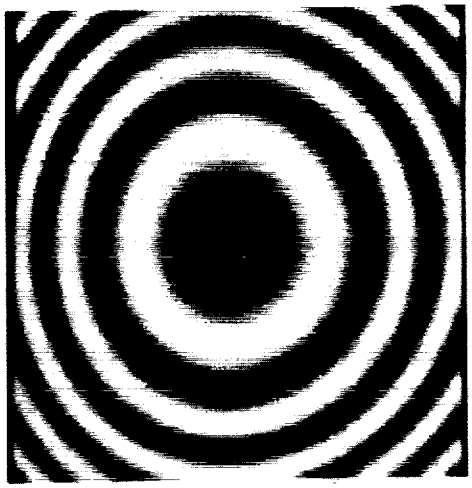

(a.)

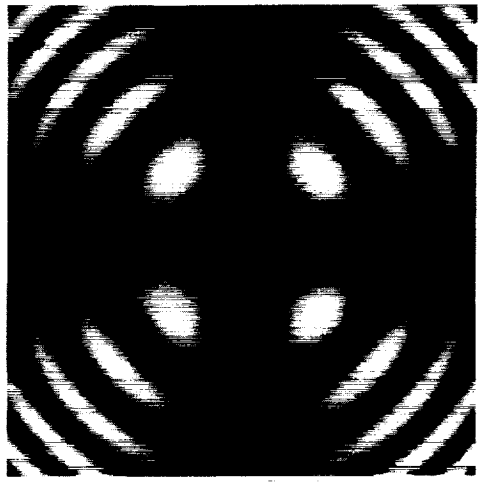

(b.)

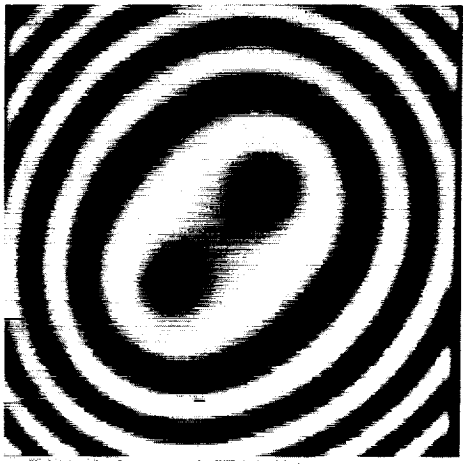

(c)

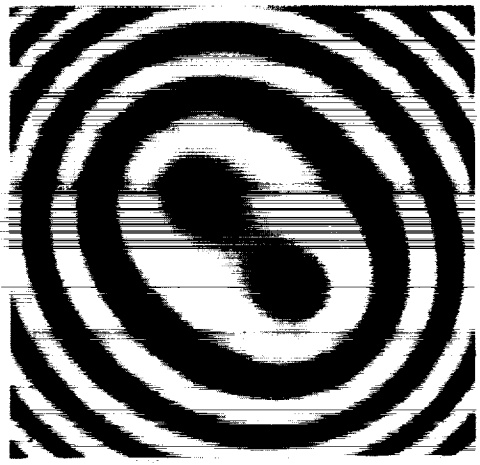

(d)

Figure 2. Polarization patterns observed when a single KD*P is between crossed polarizers. Three of the images show the polarization patterns that would be observed when a longitudinal KD*P modulator is placed between crossed circular polarizers with (a) zero (c) plus quarterwave, and (d) minus quarterwave voltages applied. The fourth image (b) shows a longitudinal KD*P modulator between crossed linear polarizers with zero voltage.

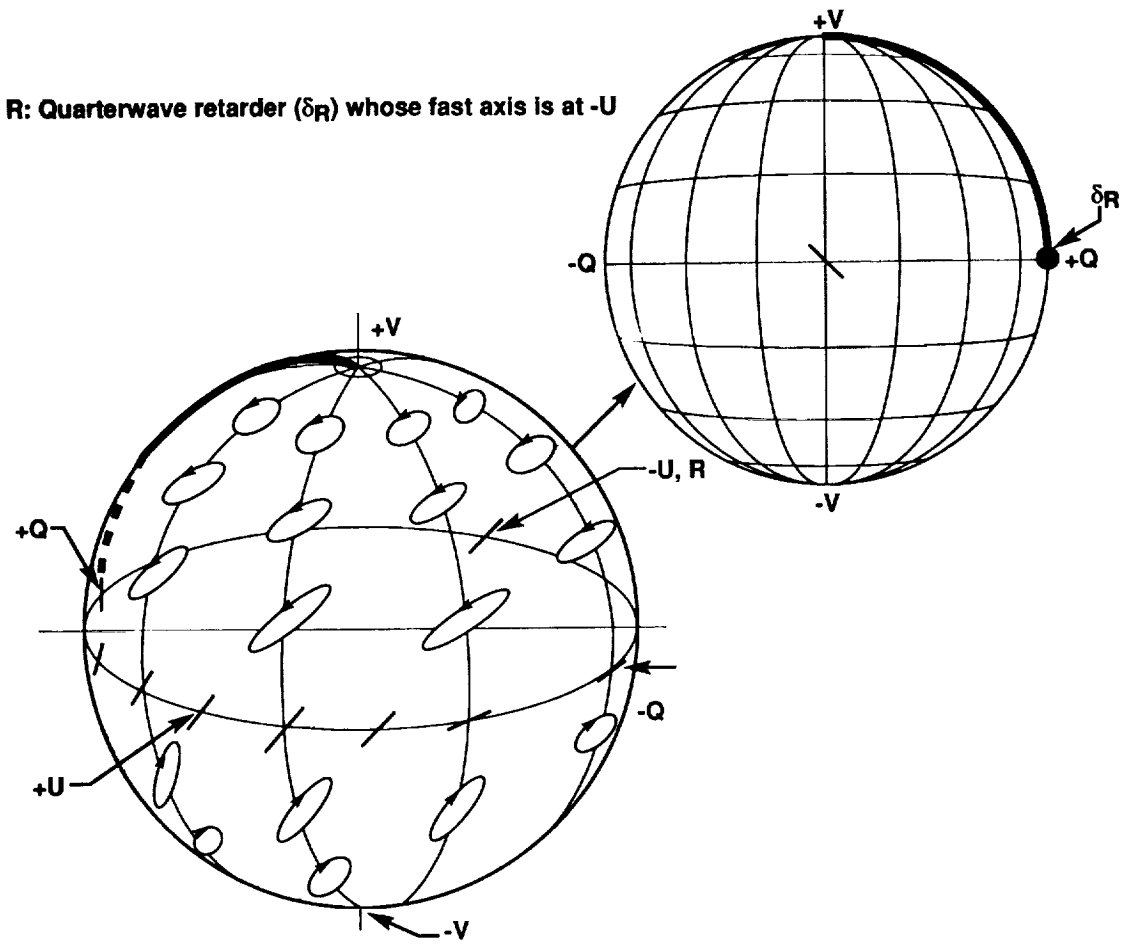

Figure 3. Mapping of the Stokes vector on the Poincaré sphere. Left and right circular polarization are at the poles of the sphere while all linear polarizations are at the equator. Two-dimensional images are placed around the sphere to help visualize the optical effect that the retarders have on polarization. When viewed at the fast axis position, all positive retardances rotate the input polarization in the clockwise direction.

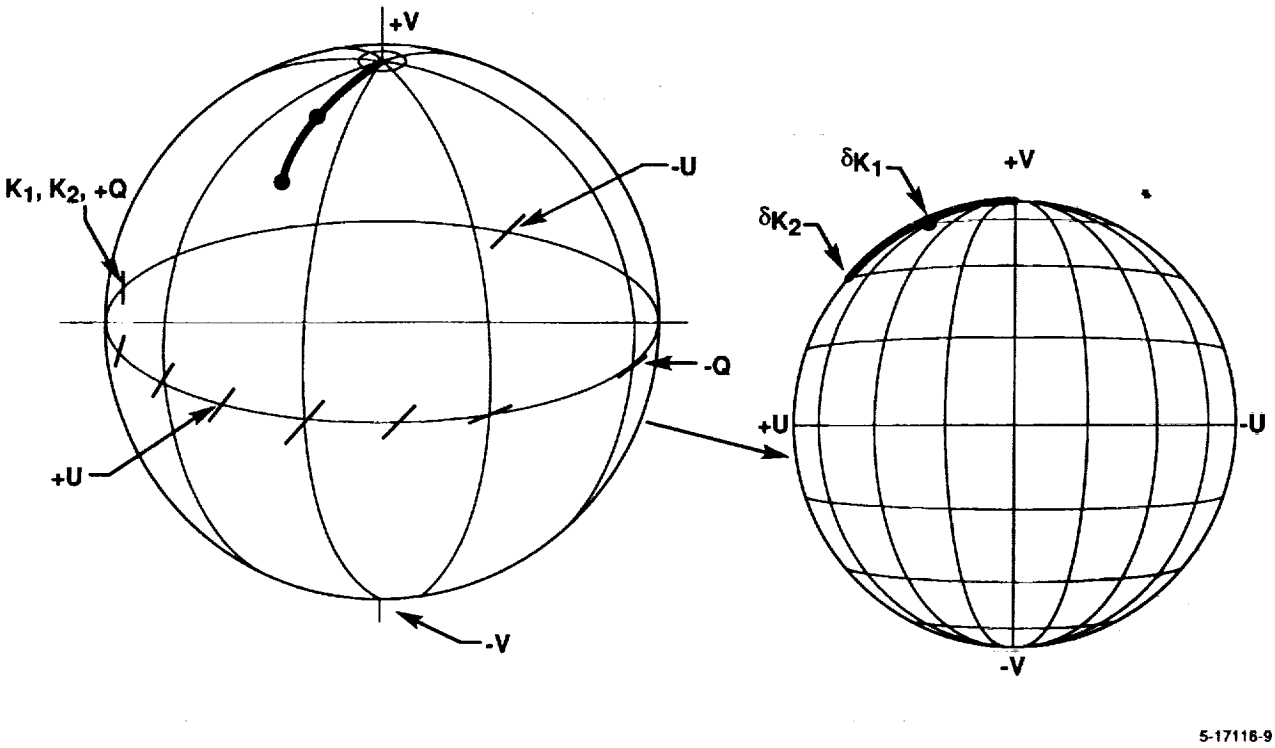

Figure 4. Using the Poincaré sphere to describe the field of view errors of two KD*Ps. Assuming that the thickness of the two KD*Ps are equal and that the optic axes are parallel, then the fast axis and the retardance for an off-axis light ray will be the same for both KD*Ps. Therefore, doubling the KD*P thickness doubles the field of view errors.

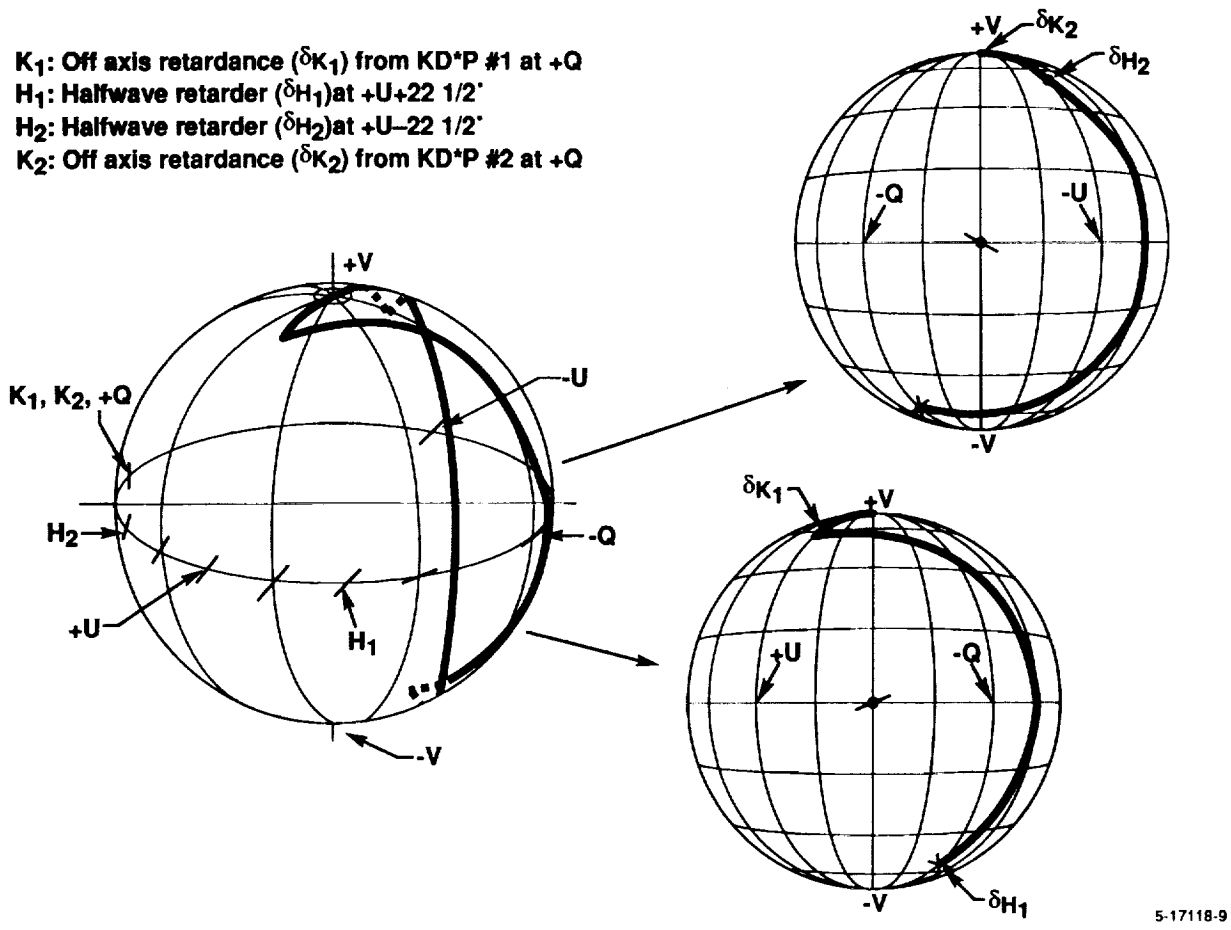

Figure 5. Using the Poincaré sphere to describe the field of view errors of a two KD*P, two halfwave plate modulator (no applied voltage). Assuming the KD*P thicknesses are equal and the optic axes are parallel, the error from the first KD*P is rotated by the halfwave plates to a position on the Poincaré sphere such that the error of the second KD*P cancels the first.

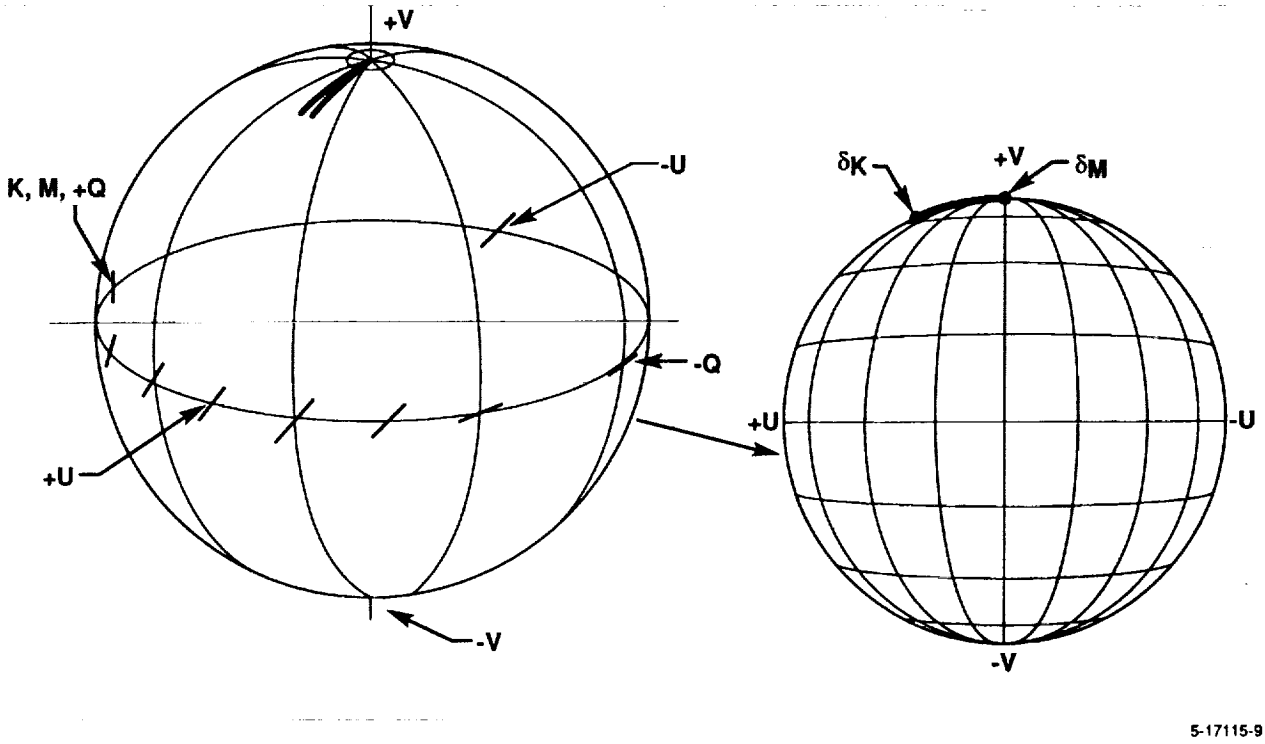

Figure 6. Using the Poincaré sphere to describe the field of view errors of a KD*P, MgF_2 modulator (no applied voltage). Assuming that the optic axes are parallel and that the thickness of the MgF_2 is ≈ 3.0 times the thickness of the KD*P crystal, the off-axis error of the MgF_2 crystal cancels the error of the KD*P. crystal.

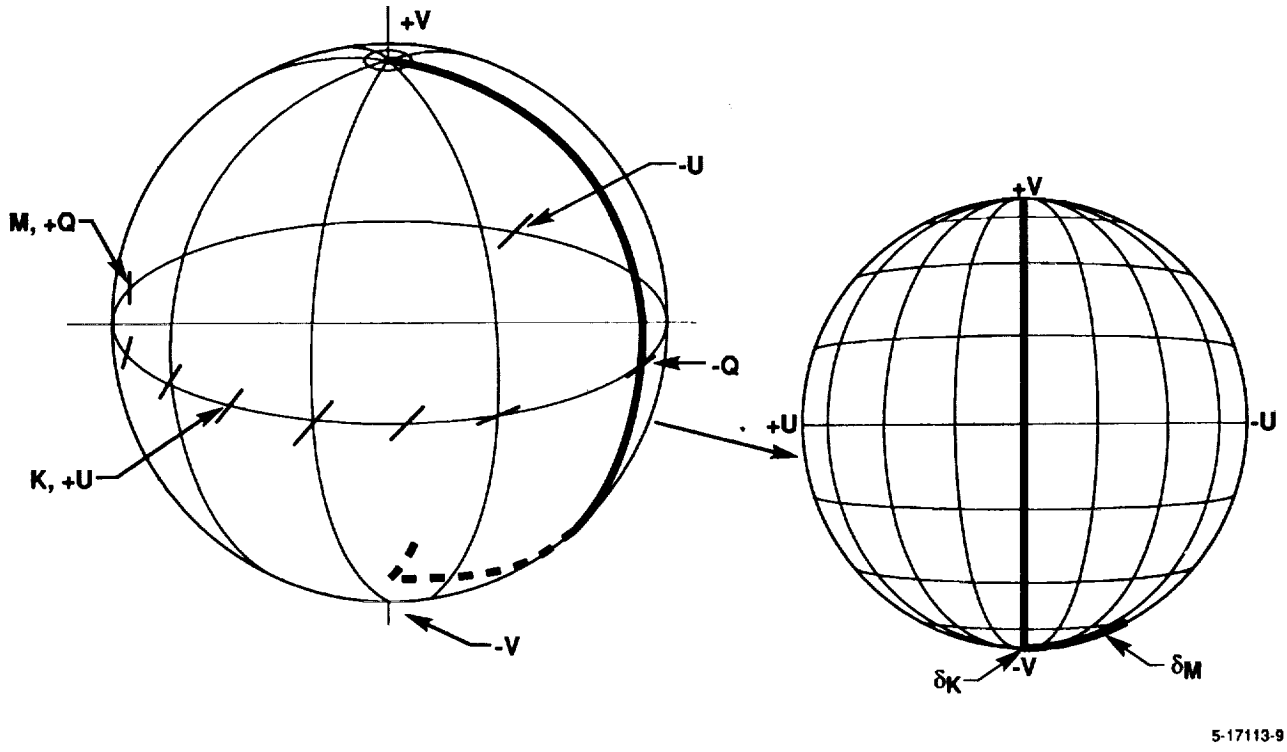

Figure 7. Using the Poincaré sphere to describe the field of view errors of a KD*P, MgF_2 modulator (applied voltage = 180° retardance). For small off-axis angles, an applied electric field will rotate the fast axis to the $+U$ position. While the off-axis error from the KD*P changes, the MgF_2 errors remains the same. Therefore, the field of view errors return with the applied voltage.

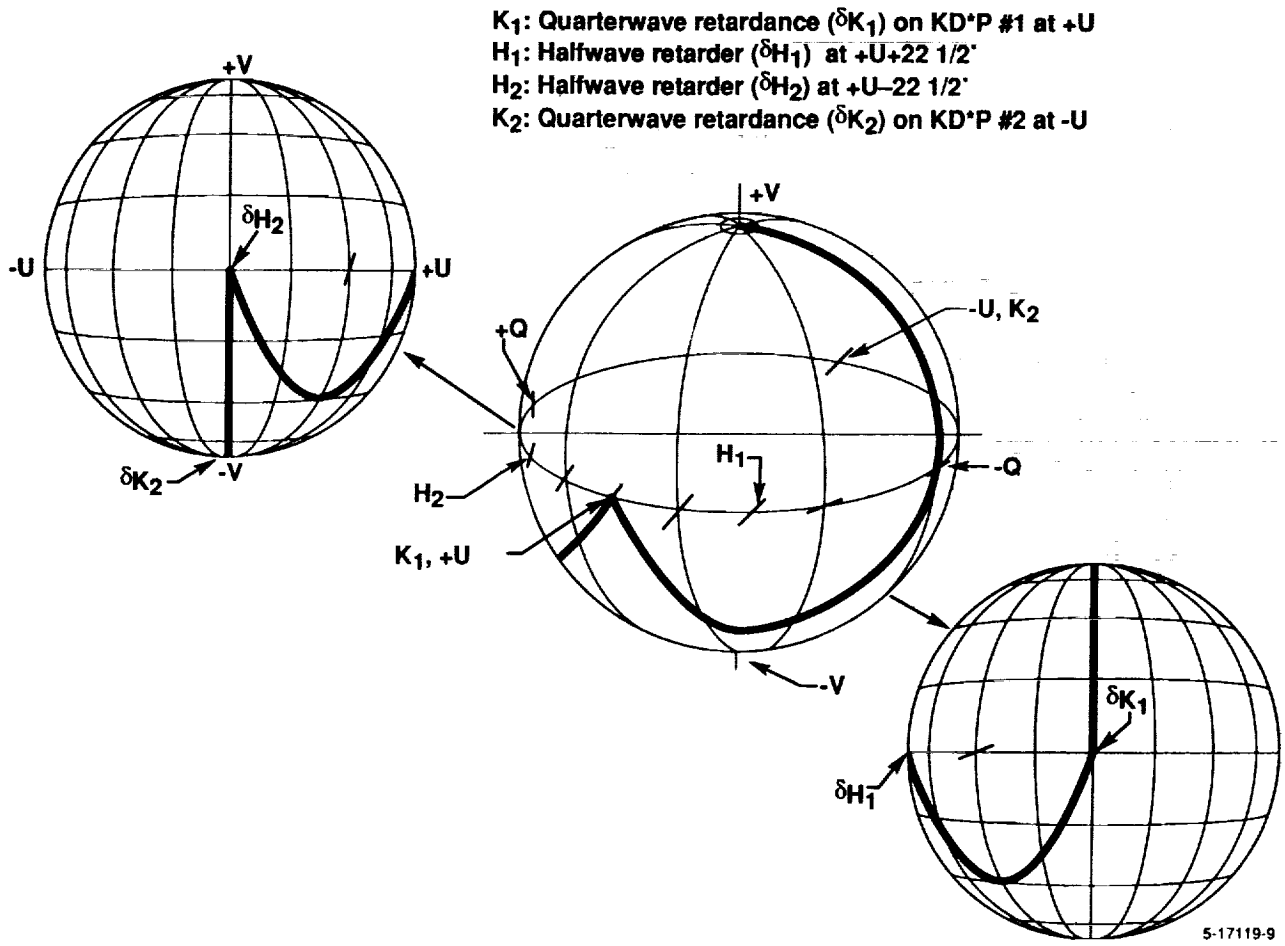

Figure 8. Using the Poincaré sphere to describe the field of view errors of a two KD*P, two halfwave plate modulator (applied voltage = +90 ° on KD*P_1, -90° on KD*P_2 retardance). For small off-axis angles, the off-axis errors are assumed to be small when compared to the voltage induced retardation. Therefore the left circular polarization ($+V$) is transformed to right ($-V$) with no field of view errors ($+Q$, $+U$ components).

Modulator Name	Optical Alignment	Modulation Scheme	Measured Polarization (A–B)
Single KD*P	S 45°	A = +90°	+V
	KD*P	B = -90°	
Single M_gF_2	S 45° ⊙	A = +90°	+V
	KD*P M_gF_2	B = -90°	
Split M_gF_2	⊙ S 45° ⊙	A = +90°	+V
	M_gF_2 KD*P M_gF_2	B = -90°	
Crossed KD*P	S 45° S 67 1/2° F F 45°	A = 0°	-Q
	KD*P $\lambda/2$ $\lambda/2$ KD*P	B = 90°	
Crossed M_gF_2	⊙ S 45° ⊙ S 67 1/2° F ⊙ F 45° ⊙	A = 0°	-Q
	M_gF_2 KD*P M_gF_2 $\lambda/2$ $\lambda/2$ M_gF_2 KD*P M_gF_2	B = 90°	

⊙ – Optic axis parallel to incident light

Figure 9. Descritpion of the five modulator designs that will be studied

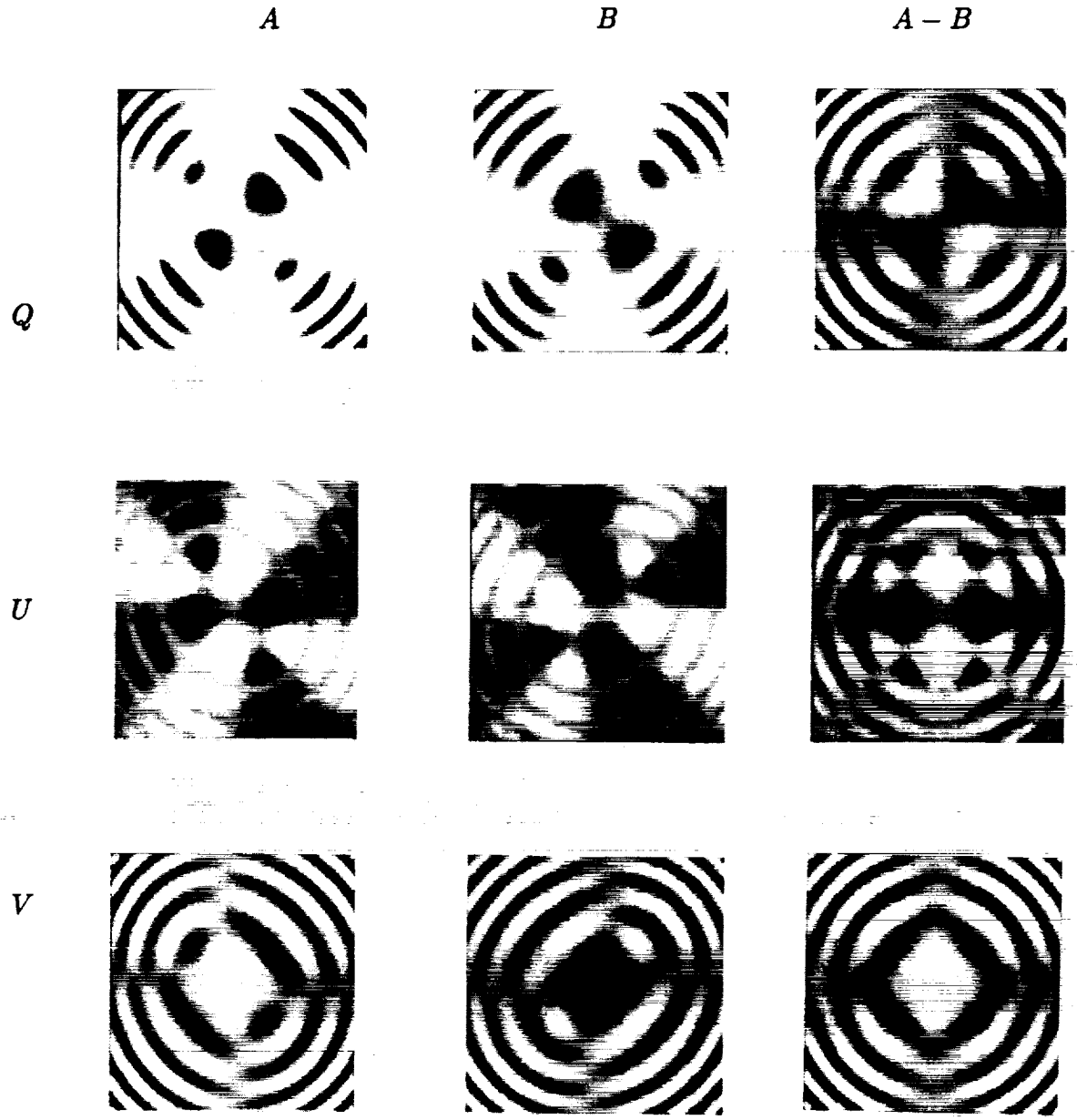

Figure 10. Polarization patterns created by the *single* KD*P modulator described in Figure 9. The field of view is $\pm 10°$ in both the X and Y axis. The polarization maps for the two modulator positions ($A = +90°$, $B = -90°$) are scaled from 0.0 to 1.0 while the difference maps ($D_p = A - B$, $p = Q, U, V$) are scaled between ± 1.0.

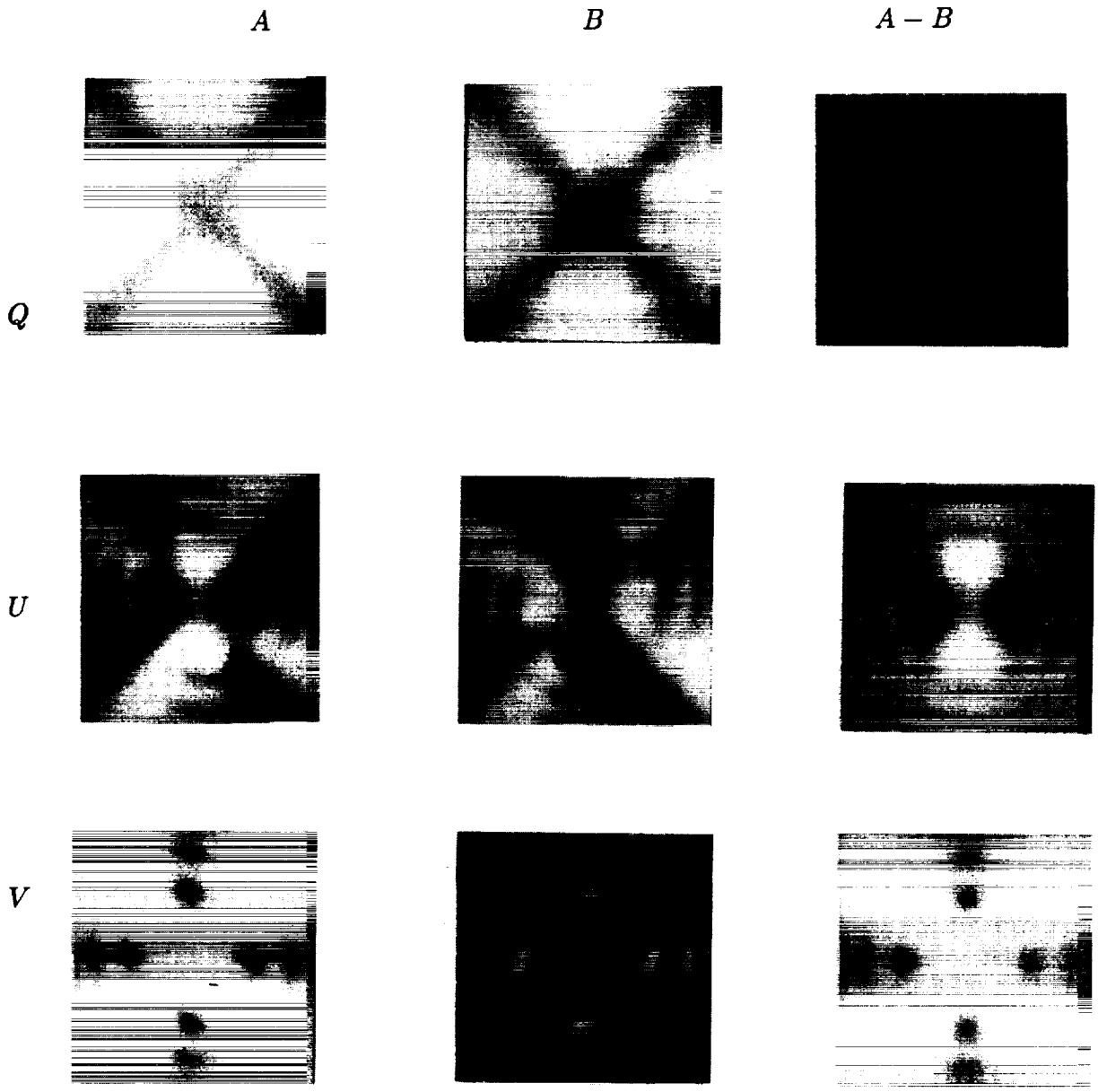

Figure 11. Polarization patterns created the *single* MgF_2 modulator described in Figure 9. The field of view is $\pm 10°$ in both the X and Y axis. The polarization maps for the two modulator positions ($A = +90°$, $B = -90°$) are scaled from 0.0 to 1.0 while the difference maps ($D_p = A - B$, $p = Q, U, V$) are scaled between ± 1.0.

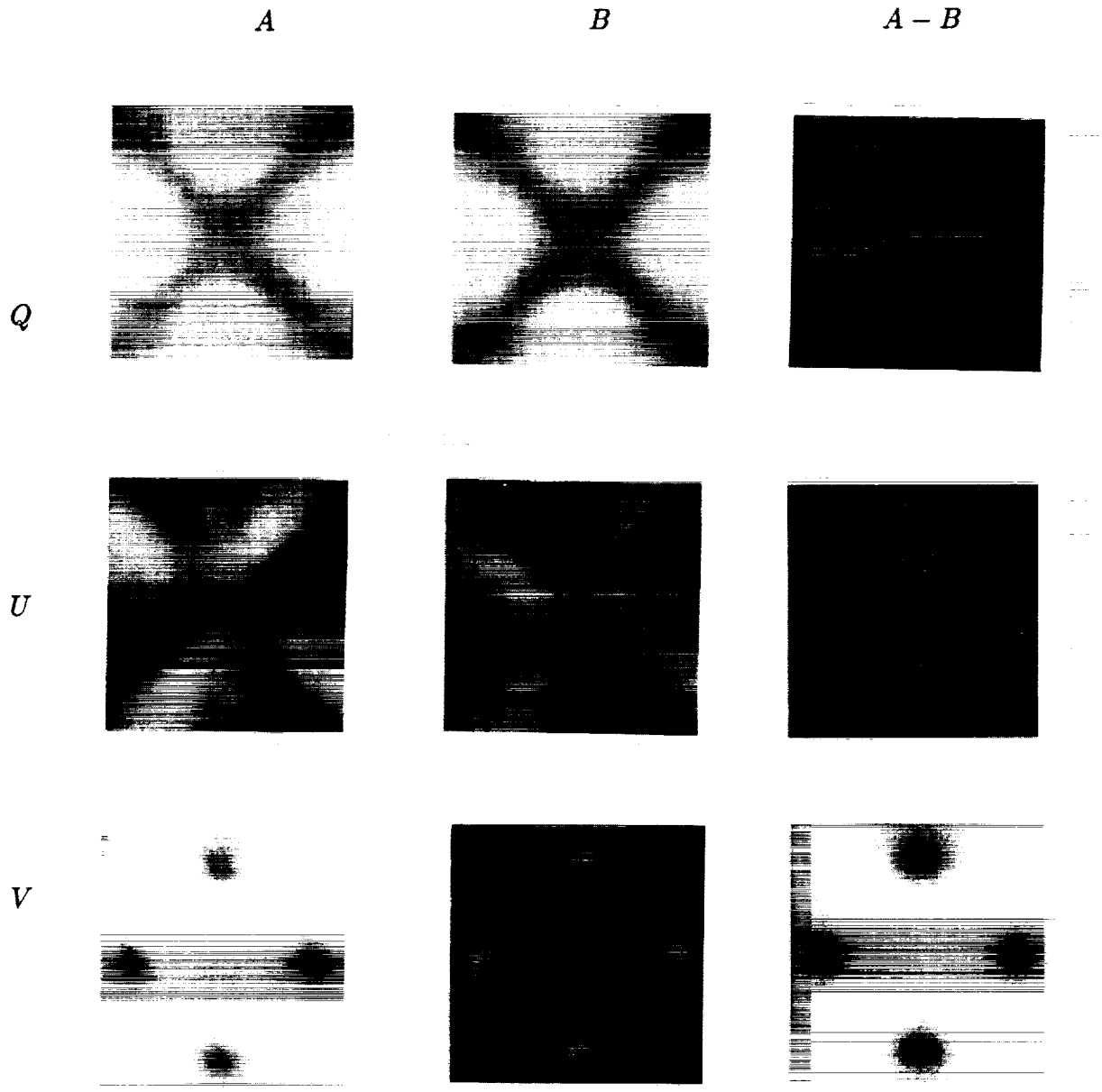

Figure 12. Polarization patterns created by the *split* MgF_2 modulator described in Figure 9. The field of view is $\pm 10°$ in both the X and Y axis. The polarization maps for the two modulator positions ($A = +90°$, $B = -90°$) are scaled from 0.0 to 1.0 while the difference maps ($D_p = A - B$, $p = Q, U, V$) are scaled between ± 1.0.

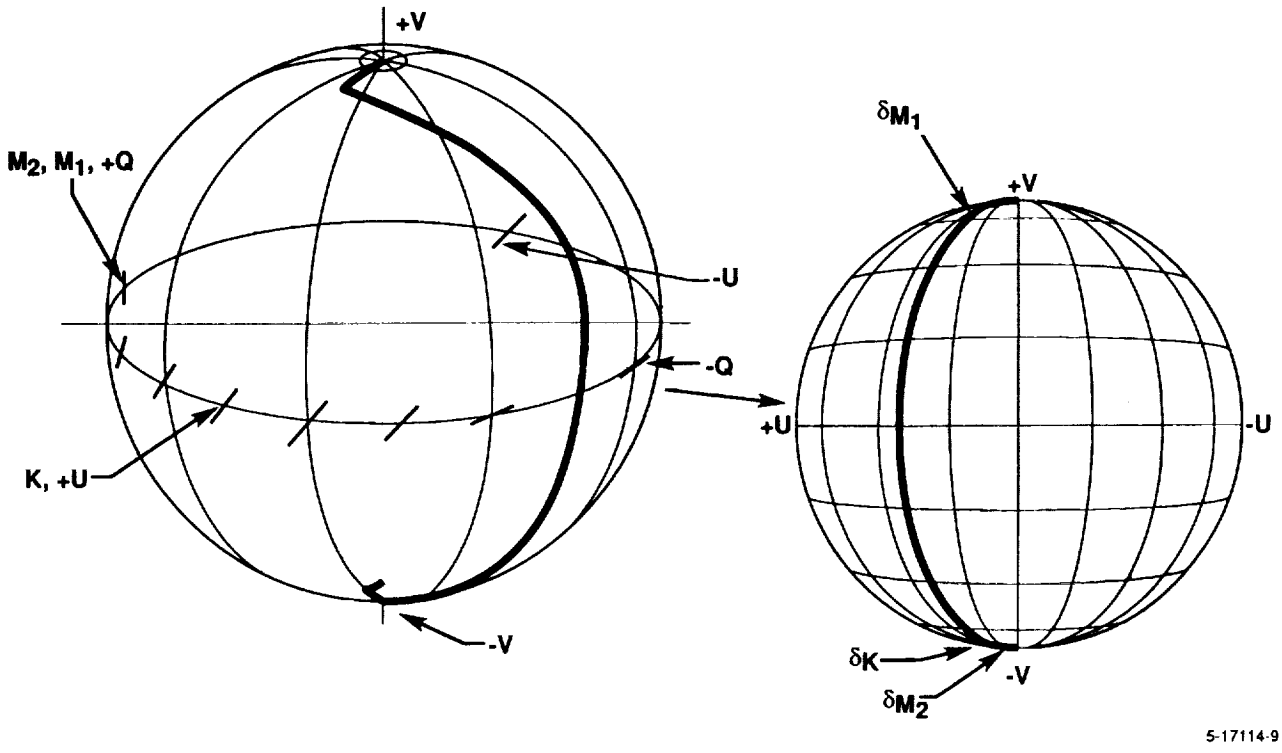

Figure 13. Using the Poincaré sphere to describe the field of view errors of a *split* MgF_2 modulator (applied voltage = 180° retardance). For small off-axis angles, an applied electric field will rotate the fast axis of the KD*P to the $+U$ position. In this case the error produced by the first MgF_2 plate is rotated to a position on the Poincaré sphere such that the errors from the two MgF_2 crystals cancel out.

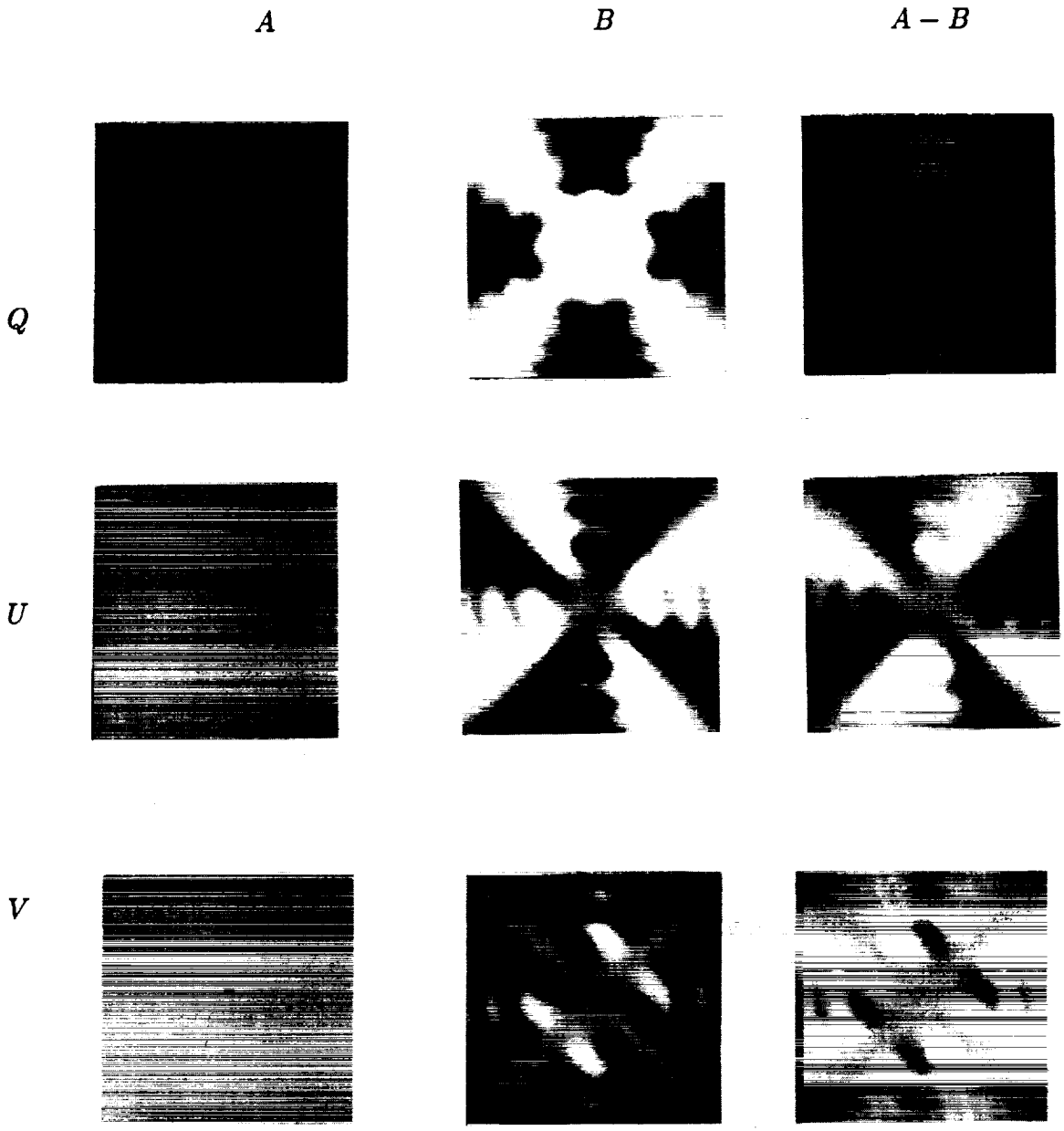

Figure 14. Polarization patterns created by the *crossed* KD*P modulator described in Figure 9. The field of view is $\pm 10°$ in both the X and Y axis. The polarization maps for the two modulator positions ($A = 0°,\ B = +90°$) are scaled from 0.0 to 1.0 while the difference maps ($D_p = A - B,\ p = Q, U, V$) are scaled between ± 1.0.

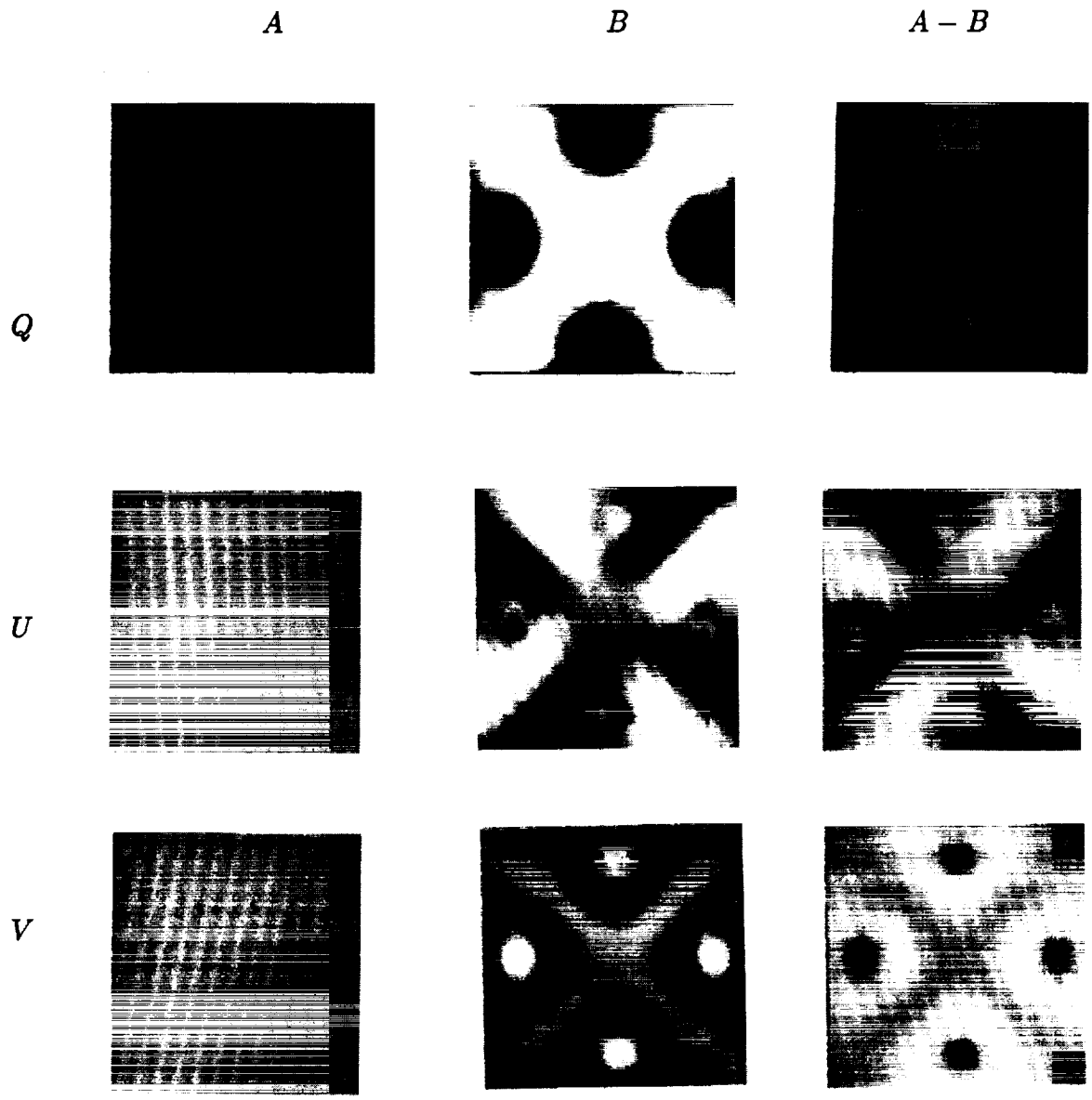

Figure 15. Polarization patterns created by the *crossed* MgF_2 modulator described in Figure 9. The field of view is $\pm 10°$ in both the X and Y axis. The polarization maps for the two modulator positions ($A = 0°$, $B = +90°$) are scaled from 0.0 to 1.0 while the difference maps ($D_p = A - B$, $p = Q, U, V$) are scaled between ± 1.0.

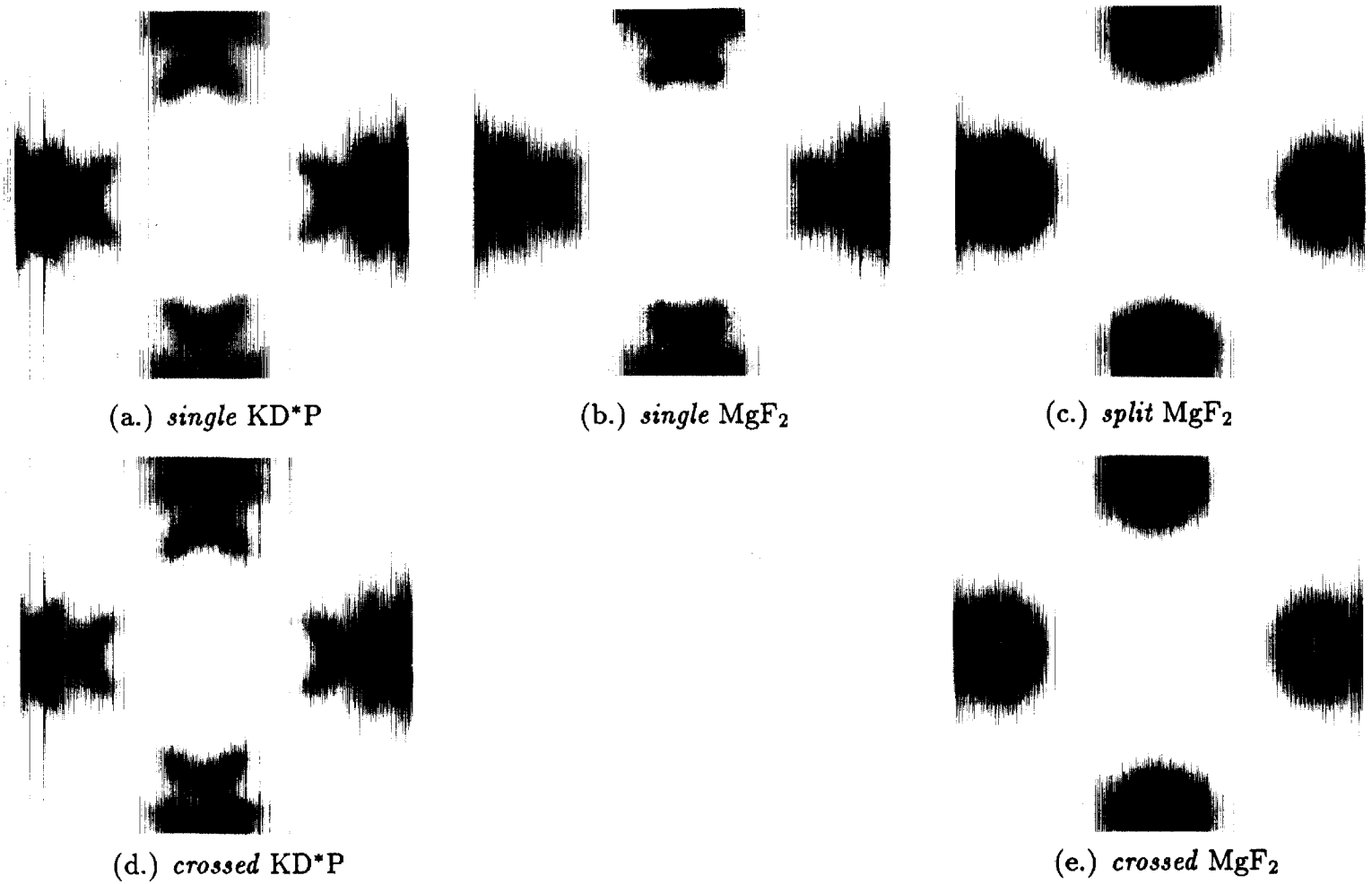

(a.) *single* KD*P (b.) *single* MgF_2 (c.) *split* MgF_2

(d.) *crossed* KD*P (e.) *crossed* MgF_2

Figure 16. Total polarization that can be measured by each KD*P modulator design. These images were created by squaring the difference image of each polarization for each modulator, summing those images, and taking the square root of the sum ($[D_Q^2 + D_U^2 + D_V^2]^{\frac{1}{2}}$ for each modulator). The images are scaled from 0.0 to 1.0.

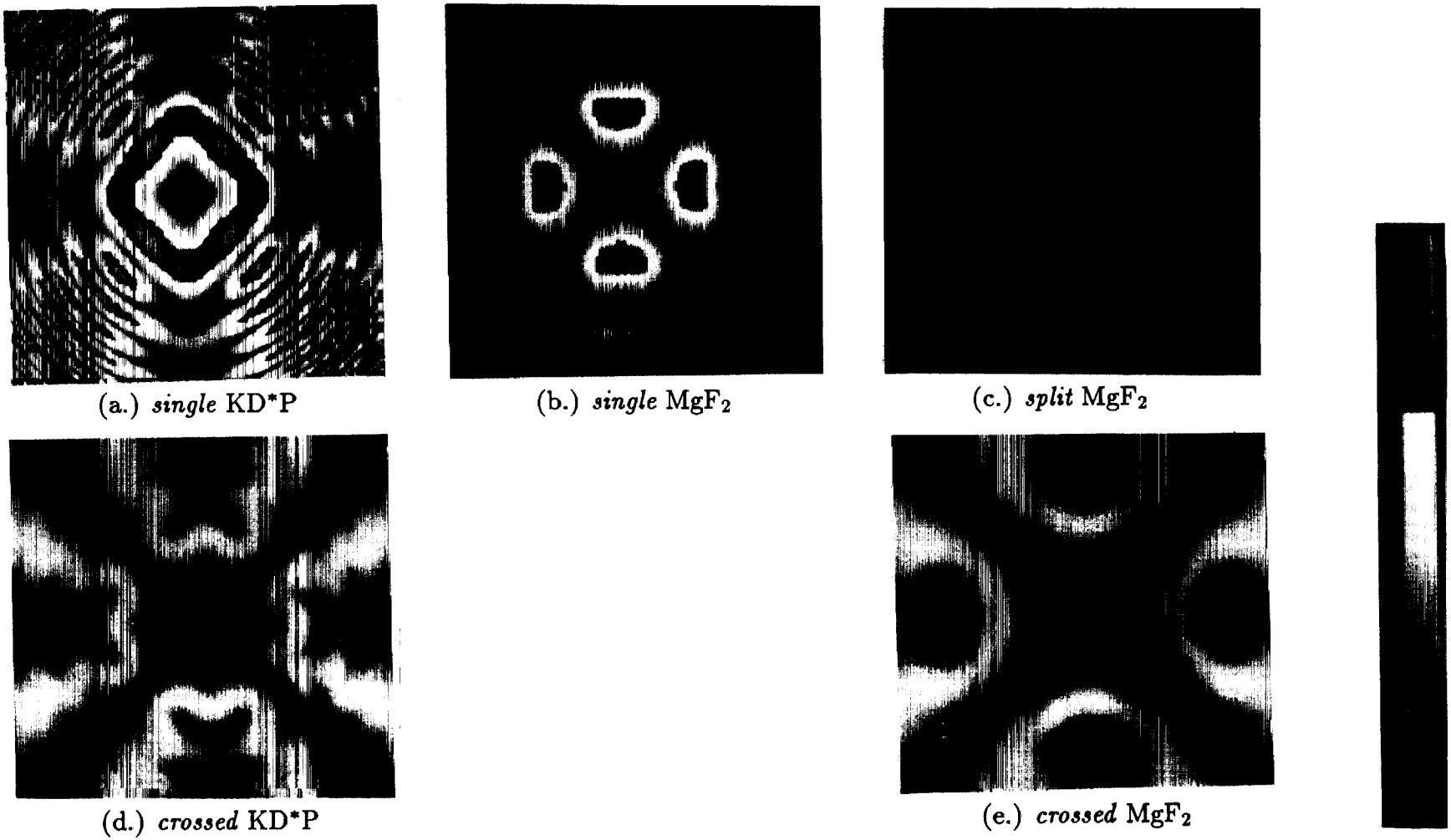

Figure 17. Polarization crosstalk that would be observed for each KD*P modulator design. These images were created by squaring the difference image of each "equal" signal polarization, summing those images, and taking the square root of the sum ($[D_Q^2 + D_U^2]^{\frac{1}{2}}$ for the *single* KD*P, the *single* MgF_2 and the *split* MgF_2 modulators; $[D_V^2 + D_U^2]^{\frac{1}{2}}$ for the *crossed* KD*P and *crossed* MgF_2 modulators). The images are scaled from 0 to 1.

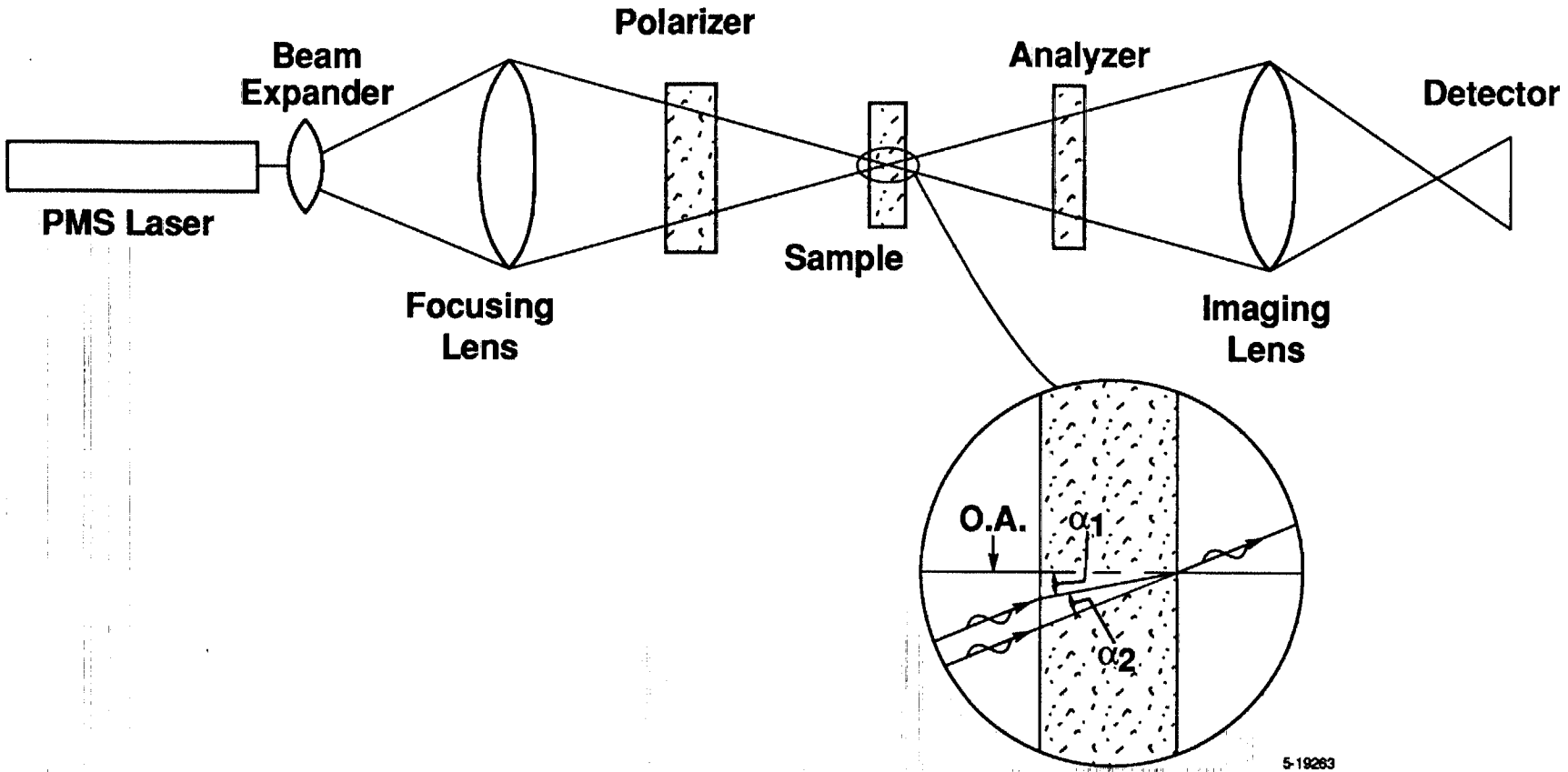

Figure 18. Optical components used in polarization testing.

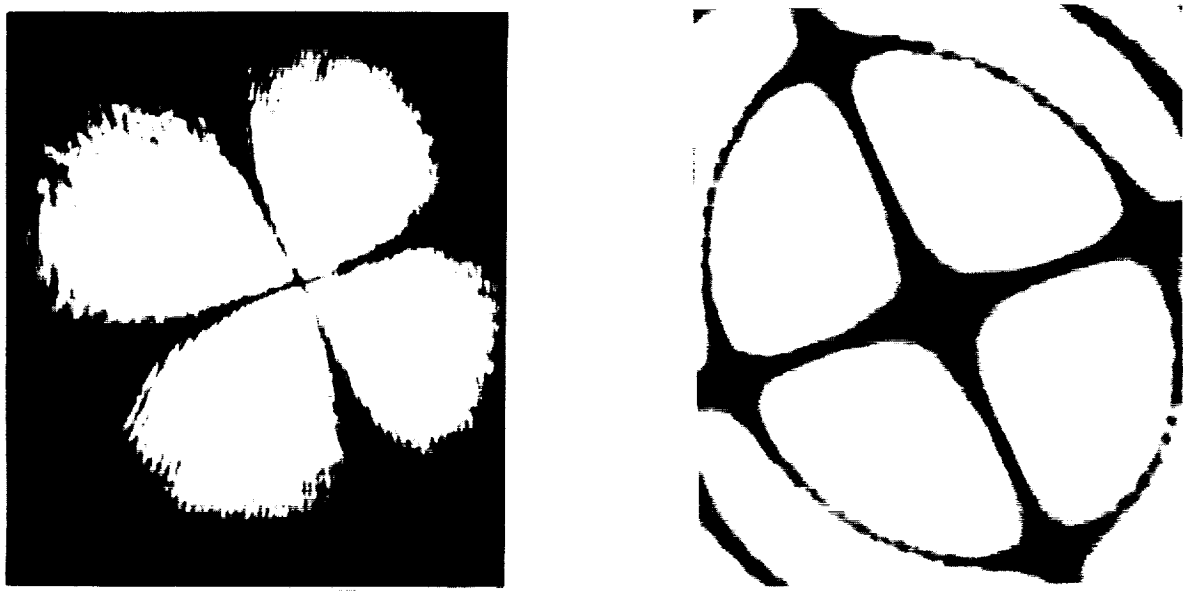

(a.) Observed (b.) Calculated

Figure 19. Observed polarization patterns of the *single* KD*P modulator with zero voltage applied. The input polarization is $-Q$, the applied voltage is zero and the field of view is approximately ± 8 degrees.

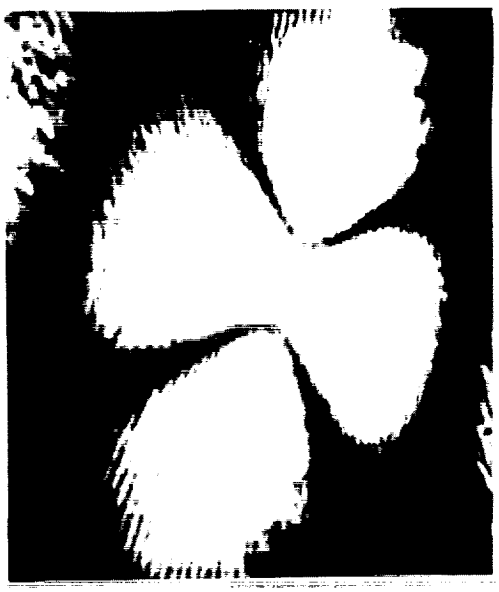

(a.) $A = +\frac{1}{4}$ voltage

(b.) $B = -\frac{1}{4}$ voltage

(c.) Observed difference

(d.) Calculated difference

Figure 20. Observed polarization patterns of the *single* KD*P modulator with applied voltages. The input polarization is $-Q$. The difference images are created by subtracting the B image from the A image. The image scale and saturation levels are the same as those in Figure 19.

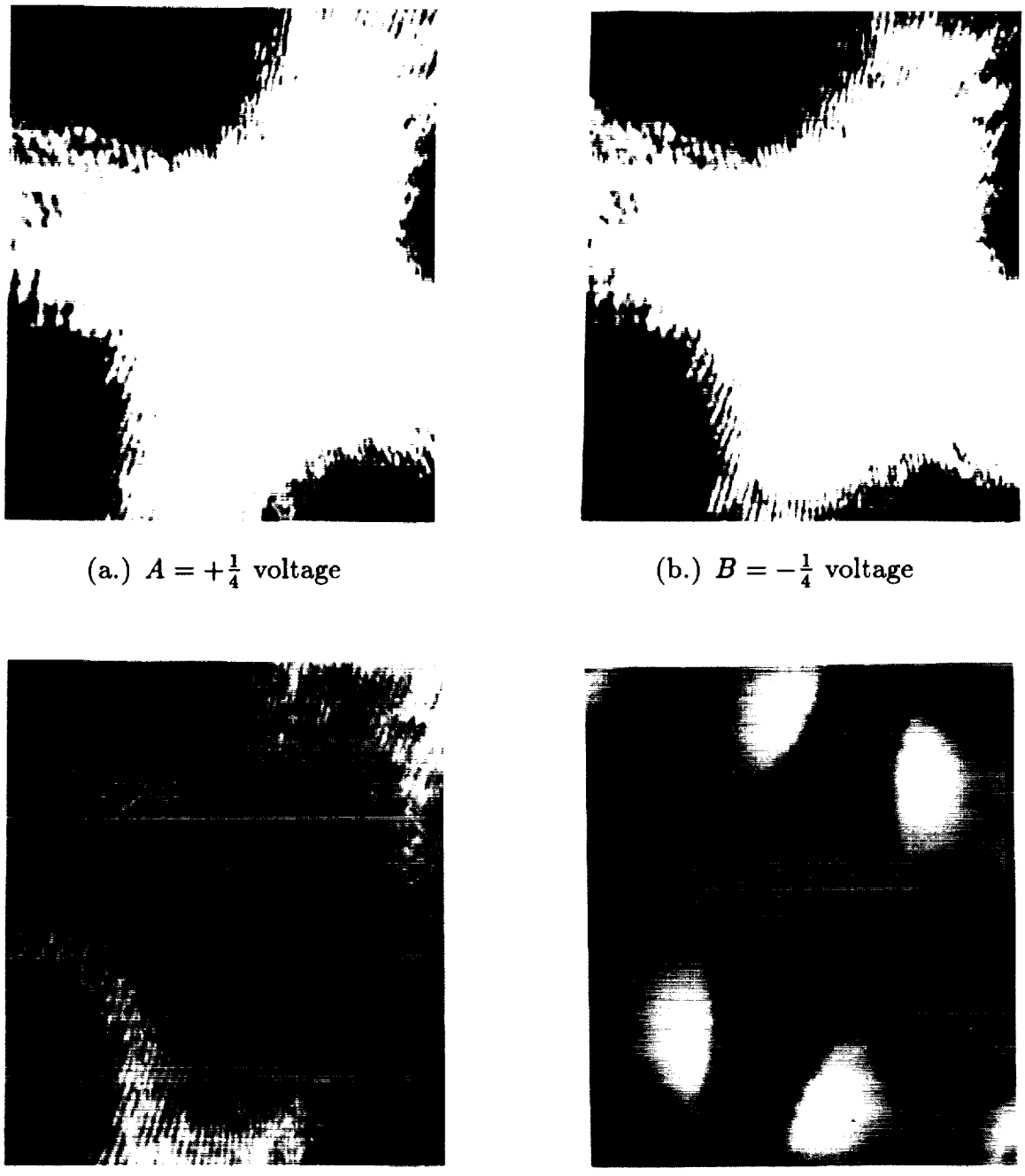

(a.) $A = +\frac{1}{4}$ voltage

(b.) $B = -\frac{1}{4}$ voltage

(c.) Observed difference

(d.) Calculated difference

Figure 21. Observed polarization patterns of the *split* MgF_2 modulator with applied voltages. The input polarization is $-Q$. The difference images are created by subtracting the B image from the A image. The image scale and saturation levels are the same as those in Figure 19.

Table 1. CONSTANTS USED TO CALCULATE POLARIZATION PATTERNS

Material	Indices of refraction $\lambda = 6234$ Å		Electro-optic coefficient (m/V)
	n_e	n_o	
KD*P	1.46560 (Phillips, 1966)	1.50440	26.4×10^{-12} (Sliker and Burlage, 1963)
MgF_2	1.38858 (Wolfe, 1978)	1.37682	0.0

Table 2. THICKNESS DATA FOR KD*P CRYSTALS USED IN MODULATOR TESTING

KD*P No.	Wavelength (Å)	180° minimum (cm)	Estimated thickness (mm)	360° minimum (cm)	Estimated thickness (mm)
12595-1	5430	37.46	2.68	52.30	2.78
	5941	39.08	2.72	55.35	2.76
	6119	39.39	2.77	55.60	2.83
	6234	40.44	2.69	57.35	2.72
12595-2	5430	36.10	2.88	50.67	2.96
	5941	38.02	2.88	53.35	2.96
	6119	38.59	2.89	54.10	2.98
	6234	39.14	2.87	55.30	2.92
5-2	5430	31.35	3.81	44.47	3.82
	5941	32.50	3.92	46.10	3.93
	6119	33.38	3.85	47.37	3.86
	6234	33.70	3.85	47.60	3.91
9-4	5430	33.86	2.92	52.25	2.79
	5941	38.20	2.84	53.87	2.90
	6119	38.49	2.90	55.30	2.86
	6234	39.47	2.82	56.00	2.85

REFERENCES

Guo-Xaing, Ai and Hu Yue-Feng, 1981, "The KD*P Modulator in the Solar Magnetic Field Telescope," Tianti Wuli Xuebao, **1**, (4), 273.

Hagyard, M. J., E. A. West and N. P. Cumings, 1984, "The New MSFC Vector Magnetograph," NASA TM-82568.

Klein, Miles V., 1970, Optics, John Wiley and Sons, Inc., p. 610.

Phillips, Richard A., 1966, "Temperature Variation of the Index of Refraction of ADP, KDP and Deuterated KDP*," Journal of the Optical Society of America **56**, no. 5, 631.

Shurcliff, William A., 1966, Polarized Light, Harvard University Press, 19.

Sliker, T. R. and S. R. Burlage, 1963, " Some dielectric and optical properties of KD_2PO_4," Journal of Applied Physics, **34**, 1837-1840.

West, Edward A., 1978, "Extending the field-of-view of KD*P electro-optic modulators," Applied Optics, **17**, 3010.

West, E. A., 1985, "Analysis of the New Polarimeter for the Marshall Space Flight Center Vector Magnetograph," in Measurements of Solar Vector Magnetic Fields, NASA Conference Publication 2374, p. 160.

West, E. A., 1989, "Using KD*P modulators for polarization measurements of the Sun," *Polarization Considerations for Optical Systems II*, SPIE proceedings, p. 434.

West, E. A. and S. S. Bhatia, 1990, "Optical properties of KD*P Modulators," *Polarimetery : Radar, Infrared, Visible, Ultraviolet, and X – Ray*, SPIE proceedings, p. 346.

West, Ed and Nathan Wilkins, 1992, "DC Bias Modulation Characteristics of Longitudinal KD*P Modulators," *Polarization Analysis and Measurement*, SPIE proceedings, in publication.

Wolfe, Williams L., 1978, "Properties of Optical Materials," Handbook of Optics Walter G. Driscill and William Vaughan, eds., McGraw-Hill Book Co., Chapter 7, p. 95.

APPENDIX A

The equation that describes the index ellipsoid for longitudinal KD*P modulators is:

$$\left(\frac{x}{n_o}\right)^2 + \left(\frac{y}{n_o}\right)^2 + \left(\frac{z}{n_e}\right)^2 + 2r_{63}E_z xy = 1 \tag{1}$$

where x, y, and z represent normalized crystallographic axes, n_o and n_e are the ordinary and extraordinary indices of refraction, and r_{63} is the electro-optic coefficient for the applied electric field in the z direction (E_z).

A new coordinate system is defined for light traveling at an angle to the optic axis (z).

$$\begin{bmatrix} x \\ y \\ z \end{bmatrix} = \begin{bmatrix} cos\beta & sin\beta sin\alpha & sin\beta cos\alpha \\ 0 & cos\alpha & -sin\alpha \\ -sin\beta & cos\beta sin\alpha & cos\beta cos\alpha \end{bmatrix} \begin{bmatrix} x_1 \\ y_1 \\ z_1 \end{bmatrix} \tag{2}$$

The equation describing the indices of refraction for light traveling in the z_1 direction can be found by setting z_1 to zero. Using equations (1) and (2) and setting z_1 to zero gives:

$$A_1 {x_1}^2 + A_2 x_1 y_1 + A_3 {y_1}^2 = 1 \tag{3}$$

where

$$A_1 = \left(\frac{1}{n_o}\right)^2 cos^2\beta + \left(\frac{1}{n_e}\right)^2 sin^2\beta \tag{4a}$$

$$A_2 = \left(\frac{1}{{n_o}^2} - \frac{1}{{n_e}^2}\right) sin2\beta sin\alpha + 2r_{63}E_z cos\beta cos\alpha \tag{4b}$$

$$A_3 = \left(\frac{1}{{n_o}^2}\right)(sin^2\beta sin^2\alpha + cos^2\alpha) + \left(\frac{1}{{n_e}^2}\right) cos^2\beta sin^2\alpha + r_{63}E_z sin\beta sin2\alpha \tag{4c}$$

Equation (3) describes the intersection of a plane perpendicular to the z_1 direction and the index ellipsoid. This is the general equation for an ellipse. The major and minor axes can be found by making a second coordinate transformation:

$$\begin{bmatrix} x_1 \\ y_1 \\ z_1 \end{bmatrix} = \begin{bmatrix} cos\rho & -sin\rho & 0 \\ sin\rho & cos\rho & 0 \\ 0 & 0 & 1 \end{bmatrix} \begin{bmatrix} x_2 \\ y_2 \\ z_2 \end{bmatrix} \tag{5}$$

When

$$\rho = \frac{1}{2}cot^{-1}\left[\frac{(A_3 - A_1)}{(-A_2)}\right] \tag{6}$$

equation (3) then becomes

$$C_1 {x_2}^2 + C_2 {y_2}^2 = 1 \tag{7}$$

where

$$C_1 = A_1 cos^2\rho + A_2 cos\rho sin\rho + A_3 sin^2\rho \tag{8a}$$

$$C_2 = A_1 sin^2\rho - A_2 cos\rho sin\rho + A_3 cos^2\rho \tag{8b}$$

Finally the indices for the fast and slow axes are:

$$n_{x_2} = \frac{1}{(C_1)^{\frac{1}{2}}} \tag{9a}$$

$$n_{y_2} = \frac{1}{(C_2)^{\frac{1}{2}}} \tag{9b}$$

Therefore, for light traveling in the z' $(z_1,\ z_2)$ direction the fast axis relative to the crystallographic axes is ρ and the indices of refraction $n'_x,\ n'_y$ are: $n'_x = n_{x_2}$ and $n'_y = n_{y_2}$.

APPROVAL

DEVELOPMENT OF A LARGE FIELD-OF-VIEW KD*P MODULATOR--CENTER DIRECTOR'S DISCRETIONARY FUND FINAL REPORT (PROJECT NO. 91-23)

By

E. A. West

This report has been reviewed for technical accuracy and contains no information concerning national security or nuclear energy activities or programs. The report, in its entirety, is unclassified.

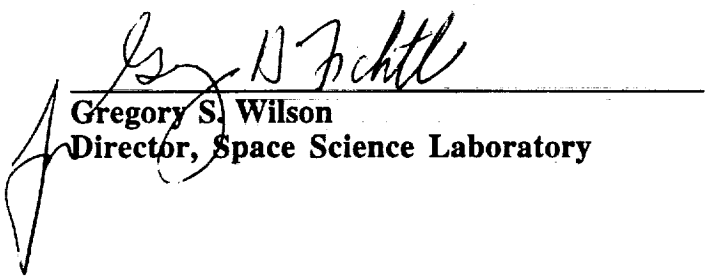

Gregory S. Wilson
Director, Space Science Laboratory

☆ US. GOVERNMENT PRINTING OFFICE 1993–733-050/80087